

WALLABY pilot survey: an ‘almost’ dark cloud near the Hydra cluster

T. O’Beirne^{1,2}★, L. Staveley-Smith^{1,2}, O. I. Wong^{1,2,3}, T. Westmeier^{1,2}, G. Batten⁴, V. A. Kilborn⁴, K. Lee-Waddell^{1,3,5}, P. E. Mancera Piña⁶, J. Román^{7,8}, L. Verdes-Montenegro⁹, B. Catinella^{1,2}, L. Cortese^{1,2}, N. Deg¹⁰, H. Dénes¹¹, B. Q. For^{1,2}, P. Kamphuis¹², B. S. Koribalski^{13,14}, C. Murugesan^{2,3}, J. Rhee¹, K. Spekkens¹⁵, J. Wang¹⁶, K. Bekki¹ and Á. R. López-Sánchez^{1,2,17,18}

Affiliations are listed at the end of the paper

Accepted 2024 January 17. Received 2023 December 22; in original form 2023 August 20

ABSTRACT

We explore the properties of an ‘almost’ dark cloud of neutral hydrogen (HI) using data from the Widefield ASKAP L-band Legacy All-sky Survey (WALLABY). Until recently, WALLABY J103508 – 283427 (also known as H1032 – 2819 or LEDA 2793457) was not known to have an optical counterpart, but we have identified an extremely faint optical counterpart in the Dark Energy Spectroscopic Instrument (DESI) Legacy Imaging Survey Data Release 10. We measured the mean *g*-band surface brightness to be 27.0 ± 0.3 mag arcsec⁻². The WALLABY data revealed the cloud to be closely associated with the interacting group Klemola 13 (also known as HIPASS J1034 – 28 and the Tol 9 group), which itself is associated with the Hydra cluster. In addition to WALLABY J103508 – 283427/H1032 – 2819, Klemola 13 contains 10 known significant galaxies and almost half of the total HI gas is beyond the optical limits of the galaxies. By combining the new WALLABY data with archival data from the Australia Telescope Compact Array, we investigate the HI distribution and kinematics of the system. We discuss the relative role of tidal interactions and ram pressure stripping in the formation of the cloud and the evolution of the system. The ease of detection of this cloud and intragroup gas is due to the sensitivity, resolution, and wide field of view of WALLABY, and showcases the potential of the full WALLABY survey to detect many more examples.

Key words: surveys – galaxies: evolution – galaxies: groups: individual: Klemola 13 – galaxies: interactions – galaxies: kinematics and dynamics.

1 INTRODUCTION

With the new generation of deep, large area surveys, for example, the Arecibo Legacy Fast ALFA (ALFALFA, Giovanelli et al. 2005), the DESI Legacy Imaging Survey Data Release 10 (hereafter referred to as the Legacy Survey DR10; Dey et al. 2019), the low surface brightness universe is beginning to be explored. Ultra-diffuse galaxies (UDGs) are extremely faint and diffuse galaxies. There are several proposed definitions (e.g. Koda et al. 2015; Lim et al. 2020), with one of the most commonly used definitions being that of van Dokkum et al. (2015): galaxies with a central surface brightness $\mu_{0,g} \geq 24$ mag arcsec⁻² and an effective radius $r_{\text{eff}} \geq 1.5$ kpc. van Dokkum et al. (2015) proposed that UDGs are ‘failed’ galaxies that were prevented from becoming typical galaxies due to a loss of their gas supply early in their lifetime. In recent years, UDGs have been observed to have a range of properties and environments, from the red cluster UDGs of Koda et al. (2015), van Dokkum et al. (2015), van der Burg, Muzzin & Hoekstra (2016), and Mancera Piña et al. (2019) to the isolated HI bearing UDGs (HUDs) of Leisman et al. (2017) and Mancera Piña et al. (2020). In order to explain the variety in observed properties, various formation mechanisms have

been theorized including internal mechanisms, mergers, and tidal interactions (see Jiang et al. 2019; Sales et al. 2020; Jones et al. 2021; La Marca et al. 2022, for summaries). La Marca et al. (2022) found 11 new UDGs within $0.4r_{\text{vir}}$ of the Hydra Cluster, bringing the total number of UDGs in the Hydra cluster to 21, including the UDGs found in Iodice et al. (2020, 2021). Due to their diffuse nature, UDGs have historically been very difficult to detect, but with recent surveys this is changing. Using the Legacy Survey, Zaritsky et al. (2022) found 5598 UDG candidates which make up the Systematically Measuring Ultra-Diffuse Galaxies catalogue.

At the extreme end of low surface brightness galaxies, lie dark galaxies. Dark galaxies are isolated, dark-matter-dominated systems without optical counterparts. They are predicted by lambda-cold dark matter cosmology (e.g. Boylan-Kolchin, Bullock & Kaplinghat 2011), and those that contain HI have the potential to be detected by radio telescopes. However, they have been shown to be rare by recent studies (e.g. Kilborn et al. 2000; Janowiecki et al. 2015; Bílek et al. 2020; Wong et al. 2021), and their existence is even contested (e.g. Bekki, Koribalski & Kilborn 2005; Taylor & Webster 2005). One of the first arguments for the existence of ‘almost’ dark galaxies came from Disney (1976). He argued that extremely low surface brightness galaxies were abundant in the Universe but remained below the detection limits of the instruments available at the time. He postulated that low-mass dwarf elliptical galaxies

* E-mail: tamsynobeirne.astro@gmail.com

could just be the tip of giant low surface brightness spirals, dubbing these objects ‘crouching giants’ (Disney & Phillipps 1987). Modern cosmological simulations support the existence of dark galaxies and extremely low surface brightness galaxies. The presence of dark matter haloes without significant stellar mass (dark galaxies) is a common explanation of the ‘missing satellites’ and ‘too big to fail’ problems of cosmological dark matter only simulations (Klypin et al. 1999; Boylan-Kolchin et al. 2011; Sawala et al. 2016).

Although both are devoid of stars, it is useful to distinguish dark galaxies, which contain dark matter, from dark H I clouds, which predominantly contain gas. Cosmological simulations have shown that dark galaxies can have a primordial origin (e.g. Verde, Oh & Jimenez 2002; Taylor et al. 2016). In this scenario they are failed galaxies – dark matter haloes that accumulate gas that never condenses and undergoes star formation, and are often isolated. HI1225 + 01 in the Virgo Cluster contains a promising example of a dark galaxy candidate, with a surface brightness limit of $\mu_{r, AB} > 28$ mag arcsec⁻² (Matsuoka et al. 2012). On the other hand, gas-dominated clouds can form as the result of tidal stripping, such as in the Leo ring (Schneider et al. 1983), and the dark clouds discussed in Kilborn et al. (2006), Cannon et al. (2015), and Taylor et al. (2022). Lee-Waddell et al. (2014) present their Giant Meter Wave Radio Telescope observations of a gas-rich interacting group that contains an H I cloud with tidal origin. No optical counterpart had been detected in prior studies, but faint optical features were identified in their observations with the Canada–France–Hawaii Telescope. Clouds can also form due to ram pressure stripping (RPS), such as the plume of gas stripped from NGC 4388 in the Virgo cluster (Oosterloo & van Gorkom 2005). Both tidal interactions and RPS could have played a role in the origin of the potentially old tidal dwarf galaxy (TDG) studied in Duc et al. (2007). Often it is not possible to definitively determine whether an H I source has a primordial or interaction based origin, such as the dark clouds detected in the Eridanus group by Wong et al. (2021). The source VIRGOHI21 was initially identified in the H I Jodrell All-Sky Survey (Lang et al. 2003) data as a dark galaxy candidate (Davies et al. 2004; Minchin et al. 2005). Additional data from Arecibo led Haynes, Giovanelli & Kent (2007) to conclude that the dark source actually formed via harassment of NGC 4254. Subsequently, the system was modelled by Duc & Bournaud (2008), who show that instead of a primordial origin, the source may have been formed by a high velocity encounter between two galaxies.

TDGs form from the debris left by mergers and interacting galaxies. They are self-gravitating and do not contain a significant amount of dark matter (e.g. Bournaud & Duc 2006). In their study of TDGs in the local Universe, Kaviraj et al. (2012) found that TDGs have stellar masses less than 10 per cent of their parent galaxies and lie within 15 optical half-light radii of the parent galaxies. They also found that they contain both old stars drawn from their parent galaxies, as well as newly formed stars. Gray et al. (2023) analysed several ‘almost’ dark galaxies from ALFALFA and found two TDGs at a later stage of their evolution, lying further from their potential parent galaxies. The ALFALFA almost dark galaxy studied in Leisman et al. (2021) is also shown to likely be a TDG. Román et al. (2021) show that a TDG in Hickson Compact Group 16 has similar properties to UDGs and with ~ 2 Gyr of evolution could become undetectable in the optical, matching the observational properties of a dark galaxy.

H I observations are particularly useful for investigating the evolution of galaxies as H I is typically more extended than the optical disc. H I is also a good tracer of both tidal interactions and RPS. Taylor & Webster (2005) found that in all their models dark galaxies would

have detectable H I emission. However, due to poor angular resolution and source confusion, it was difficult to definitively identify dark galaxies in the H I Parkes All Sky Survey (HIPASS, Barnes et al. 2001; Doyle et al. 2005). Less than 2 per cent of extragalactic ALFALFA sources lack an optical counterpart (Haynes et al. 2018), and many of these dark objects are associated with tidal debris (e.g. Leisman et al. 2016), with a few dark galaxy candidates followed up (e.g. Kent 2010). With the improved resolution and sensitivity of the Australian Square Kilometre Array Pathfinder (ASKAP, Hotan et al. 2021) the Widefield ASKAP L-band Legacy All-sky Survey (WALLABY, Koribalski et al. 2020) has the potential to detect dark galaxy candidates and extremely low surface brightness galaxies by being able to better locate the origin of the emission and better separate emission from other nearby objects in denser group and cluster environments. The fast survey speed will also allow more of these rare objects to be detected in the large volume covered. Inspired by the dark clouds detected in the pre-pilot data from WALLABY by Wong et al. (2021), this study began as a search for dark galaxy candidates in the phase 1 pilot WALLABY data (Westmeier et al. 2022), with six candidates being found in the Hydra field alone. Being mostly close to the noise level, follow-up observations of the candidates are necessary to confirm their reality, or otherwise. However, one of the candidates, WALLABY J103508 – 283427, has previously been detected by the Karl Jansky Very Large Array (VLA), the Nançay telescope, and the Australia Telescope Compact Array (ATCA), and is therefore a genuine detection. This paper presents analysis of WALLABY and archival data for this dark galaxy candidate alone.

WALLABY J103508-283427 was first detected with the VLA by McMahon (1993) and subsequently with Nançay (Duc et al. 1999), as H1032 – 2819. WALLABY (Westmeier et al. 2022) and archival ATCA data (López-Sánchez et al. 2008) reveal that this H I cloud is part of a complex interacting system in the Klemola 13 galaxy group (Klemola 1969, also known as HIPASS J1034 – 28 and the Tol 9 group). Klemola 13 is thought to contain the following galaxies: ESO 436 – G046, ESO 436 – IG042, ESO-LV 4360421, ESO 436 – G044, ESO 436 – G045, PGC 031288, PGC 031 270, and ESO 437 – G001 based on their similar redshifts and small projected distances. Additionally, ESO 437 – G004 and 2MASX J10355262 – 2817269 are considered to be more distant members of the group. A detailed WALLABY study of the intragroup gas and other potential clouds in the whole system is underway by Batten et al. (in preparation). López-Sánchez et al. (2008) found using their ATCA data that the H I gas in this group is predominantly located in two regions: one around the spiral galaxy ESO 436 – G046, and one around ESO 436 – IG042 (Tol 9), with the maximum H I column density found in ESO 436 – IG042. They also noted an extended arm to the north in the direction of ESO 436 – G044 and ESO 436 – G045, but did not detect any emission from these galaxies. No previous studies have been able to identify an optical counterpart for WALLABY J103508 – 283427/H1032 – 2819 (hereafter H1032 – 2819).

In this paper, we study the properties and environment of this system in depth with the addition of the new WALLABY data, and identify for the first time an extremely faint optical counterpart using the Legacy Survey DR10. The structure of this paper is as follows. In Section 2, we describe the WALLABY and archival observations, followed by Section 3 which outlines the data reduction and source finding process. The main observational results of this study are presented in Section 4, including the H I distribution and kinematics of the system, and its optical properties. Section 5 discusses the evolution of the almost dark H I cloud and the group with which it

Table 1. Observation details of the archival ATCA data (López-Sánchez et al. 2008). The time given is the on-source integration time.

Array configuration	Date	Time (h)	Total time (h)
EW352	2008 Feb 10	7.0	7.0
EW367	2008 Nov 20	5.3	7.3
	2008 Nov 21	2.0	
750A	2007 Jan 28	9.7	9.7
1.5A	2007 Jan 29	7.6	16.6
	2007 Jan 30	9.0	
6A	2008 Nov 06	9.6	9.6
Total			50.2

appears to be associated. Section 6 summarizes our findings. For the purposes of this paper, the distance to the Hydra cluster is 47.5 Mpc (Kourkchi & Tully 2017) and Klemola 13 is set to be at the same distance. The Tully–Fisher distances for the galaxies in Klemola 13 are clustered around a similar value. Throughout the paper, we adopt the AB magnitude convention.

2 DATA

2.1 ASKAP observations

This study uses data from the Hydra field of phase 1 of the WALLABY pilot survey (Westmeier et al. 2022). WALLABY is an HI survey of the local Universe ($z < 0.1$) which has been allocated 8832 h of observing time over the next five years. WALLABY is being conducted with ASKAP (Hotan et al. 2021), a radio interferometer composed of 36×12 -m dishes equipped with Phased-Array Feeds and located in Western Australia. For reasons of surface brightness sensitivity and computing requirements, the main WALLABY ASKAPsoft pipeline does not use baselines over 2 km, although a high-resolution cutout mode for pre-defined targets is currently being implemented (Murugesan et al., in preparation). With the baselines longer than 2 km removed, the angular resolution is 30 arcsec.

2.2 Archival ATCA data

Archival data from ATCA (see López-Sánchez et al. 2008) were also used in this study. ATCA is an Earth rotation aperture synthesis radio interferometer, which consists of 6×22 -m dishes, located in New South Wales, Australia. Table 1 shows the start date and integration time for each of the five array configurations used in the observations. PKS B1934 – 638 was used as the primary calibrator and PKS B1015 – 314 was used as the secondary calibrator. Across all configurations, a total of 50.2 h was spent on source. The centre frequency of the observations was 1.405 GHz with a bandwidth of 8 MHz and a frequency resolution of 15.6 kHz. The ATCA primary beam full width at half-maximum (field of view) is 34.5 arcmin. The observations were carried out in 2007 and 2008 with the pre-Compact Array Broadband Backend (pre-CABB) correlator.

2.3 Deep optical images

We use data from the DESI Legacy Imaging Surveys (Dey et al. 2019). This survey is mainly carried out with the 4 m Blanco Telescope, providing imaging in g , r , i , and z bands over a region of $>20\,000$ sq deg with seeing of the order of 1 arcsec. We use

the most recent DR10. The images were obtained from the public website of the survey (<https://www.legacysurvey.org/>). The limiting surface brightnesses were calculated on the images, with values: 29.8, 29.4, 27.7, and 28.0 mag arcsec⁻² in the g , r , i , and z bands respectively, measured in 3σ , 10×10 arcsec boxes following the depth definition by Román, Trujillo & Montes (2020). We note the considerably higher depth of the g and r bands compared to the i and z bands. These ancillary data sets are discussed in Section 4.

3 ANALYSIS

3.1 ASKAP

The data were reduced and calibrated using the ASKAPsoft pipeline (Cornwell et al. 2011; Guzman et al. 2019; Whiting 2020; Wieringa, Raja & Ord 2020). The spectral image cubes for each primary beam were deconvolved using the multiscale CLEAN algorithm (Cornwell 2008; Rau & Cornwell 2011). See Westmeier et al. (2022) for a more detailed description of the data reduction and calibration process. The rms in the final datacube is 1.6 mJy beam⁻¹, corresponding to a 3σ column density sensitivity of 1.18×10^{20} cm⁻² over 20 km s⁻¹. We apply the statistical correction to the integrated fluxes that we measure to account for the flux underestimation as outlined in Westmeier et al. (2022).

3.2 ATCA

We used the MIRIAD software package (Sault, Teuben & Wright 1995) to process the archival ATCA data. Each configuration was reduced separately and combined using the INVERT task. To reduce the data, first we flagged any radio frequency interference using UVFLAG, BLFLAG, and PGFLAG. Once we were satisfied with the quality of the data, the bandpass and phase calibration were conducted with the primary calibrator PKS B1934 – 638 and the secondary calibrator PKS B1015 – 314 using the tasks MFCAL, MFBOOT, GPCAL, and GPBOOT. Then, the continuum subtraction was performed with UVLIN. After this, the visibility data for each baseline was combined using the INVERT task, which Fourier transforms the ultraviolet (UV) data to create the dirty image. We used a cell size of 5 arcsec, an image size of 512 by 512 pixels, a velocity channel width of 20 km s⁻¹ and a robust parameter of 0.5. Antenna 6 was removed to allow us to recover the low column density intragroup gas. Longer baselines enable higher angular resolution imaging at the cost of surface brightness sensitivity. As Antenna 6 is an outlier, the resulting long baselines may not be desirable for imaging diffuse low surface brightness emission. Hence, the removal of antenna 6 will help us recover the emission on the scales that are relevant for this paper. The velocity is in the optical convention (cz) and in the heliocentric frame. For the data available and the weighting used, the estimated theoretical rms noise is 0.82 mJy. Next the deconvolution was performed using the CLEAN task, using the default MIRIAD hybrid Högbom/Clark/Steer algorithm with a cut-off of 7 mJy. The final image cube was created from the dirty image and the dirty beam using RESTOR and the primary beam correction was applied using LINMOS. The rms level of the final processed data cube at the pointing centre is 0.75 mJy, corresponding to a 3σ column density sensitivity of 1.44×10^{19} cm⁻² over 20 km s⁻¹. As the noise is not constant across the field, the rms at the centre of each aperture can be found in Table 3. The synthesized beam is 1.52×0.63 at a position angle of -2.8° .

Table 2. SoFiA parameter settings for the S + C finder (SCFIND), linker and reliability modules.

Parameter	WALLABY	ATCA	WALLABY
	Westmeier et al. (2022)	This paper	This paper
scfind.kernelsXY	0, 5, 10	0, 5, 10	0, 5, 10, 15
scfind.kernelsZ	0, 3, 7, 15	0, 3, 7, 15	0, 3, 7, 15, 31
scfind.threshold	3.5	3.9	3.5
linker.radiusXY	2	2	2
linker.radiusZ	2	2	2
linker.minSizeXY	8	8	0
linker.minSizeZ	5	5	0
reliability.threshold	0.8	0.7	0.9
reliability.scaleKernel	0.4	0.4	0.4

3.3 Source Finding

Version 2 of the Source Finding Application (SoFiA 2, Serra et al. 2015; Westmeier et al. 2021a) was used for source finding for both the ASKAP and ATCA data. In the automated pipeline used in the pilot phase 1 data release of WALLABY (Westmeier et al. 2021b), this complex interacting system was split into three separate detections and excluded some of the fainter intragroup emission. Consequently, we reran SoFiA 2 with parameters that allowed us to recover more extended emission than the automated pipeline. Table 2 outlines the important SoFiA parameter settings in the S + C (smooth and clip) finder, linker and reliability modules for the ATCA data, the automated WALLABY pipeline and our re-run. For details on these parameters see Serra et al. (2015) and Westmeier et al. (2021a). Batten et al. (in preparation) use different SoFiA parameters in order to better identify cloud candidates within the extended group emission. In all further analysis, unless otherwise stated, the WALLABY data with the SoFiA mask generated for this work has been used.

4 RESULTS

4.1 HI properties and distribution

The overall column density map of Klemola 13 created with the SoFiA mask is shown in Fig. 1, superposed on a Legacy Survey DR10 *g*-band image. The contours cover eight galaxies at similar redshifts (with velocities within 405 km s^{-1} of each other): ESO 436 – G046, ESO 436 – IG042, ESO-LV 4360421, PGC 031288, PGC 031270, ESO 436 – G044, ESO 436 – G045, and ESO 437 – G004, as well as the almost dark cloud, H1032 – 2819. ESO 437 – G001 and 2MASX J10355363 – 2817269 are at the same redshift as the rest of the system, but no HI flux is contained in the masks used here for the WALLABY and ATCA data. Fig. 1 also contains two HI clouds detected by ATCA without optical counterparts at the north western and southern edges of the image. Whilst we can neither confirm nor deny whether these clouds are genuine, it is unlikely that they are real as they lie at the edge of the ATCA field where the noise increases significantly and are undetected by WALLABY. Hence, although they are shown here for completeness, they have not been included in any subsequent analysis.

Coordinates, optical velocities, major and minor axes, and position angles for all sources with detected HI in Klemola 13 can be found in the top section of Table 3. As H1032 – 2819 and ESO 437 – G004 have a distinct separation (spatially and in velocity), elliptical apertures were created that enclosed the HI gas contained in

the SoFiA masks for both the ATCA and WALLABY data (see Fig. 4 for the masks). The position angles shown in Table 3 are the position angles of these apertures. The rest of the galaxies are surrounded by shared intragroup gas that cannot be distinctly associated with any one galaxy, so the elliptical apertures are obtained from their optical/IR dimensions. ESO 436 – IG042 and ESO-LV 4360421 are undergoing a significant interaction that is clearly visible in the optical (López-Sánchez et al. 2008). Consequently, an elliptical aperture was created that encloses the optical emission of both of these galaxies, using the position angle from López-Sánchez et al. (2008). For these galaxies, coordinates, major and minor axes were derived from the apertures. The coordinates of the rest of the sources are taken from the Two Micron All Sky Survey Extended objects (2MASX) catalogue (Skrutskie et al. 2006) and the optical velocities are from the 6dF Galaxy Survey (6dFGS) Data Release 3 (Jones et al. 2009). The major and minor axes, and the position angle of the apertures for the other four ESO galaxies (ESO 436 – G046, ESO 436 – IG042, ESO 436 – G044 and ESO 436-G045) are taken from Lauberts (1982). As these values were not available from Lauberts (1982) for PGC 031288 and PGC 031270, the major and minor axes, and position angle were derived from the values in the 2MASX catalogue. For all the other sources, the ESO optical values were on average ~ 5 times larger than their respective *K*-band 2MASX values. Hence, a factor of 5 was used to convert the *K*-band major and minor axes into an ESO-equivalent optical value for these two galaxies.

Using these optical apertures, the flux, central velocity, velocity width, and HI mass were calculated for each galaxy (and the almost dark cloud) in the system in Table 3. The central velocities measured from the ATCA data are systematically lower than those measured from the WALLABY data, particularly for the large face on spiral galaxy ESO 436 – G046. The different beam sizes and sensitivities also result in some of the smaller galaxies only being detected by one instrument. ESO 436 – G044 and ESO 436 – G045 were not detected by ATCA and PGC 031270 was not detected by WALLABY, so 3σ upper limits to the integrated flux were calculated. The two galaxies that contain the most HI are ESO 436 – G046 and ESO 437 – G004, the latter has a central velocity most similar to H1032 – 2819. The total flux and HI masses for the entire system are shown in Table 4, where the ‘intragroup gas’ refers to the HI gas in the entire system that is not contained within the apertures. A significant proportion of the gas in the system is between the galaxies rather than within their optical apertures, with only 59 per cent/52 per cent (WALLABY/ATCA) of the HI contained within the apertures, with the limitation that optically defined apertures have been used for most of the galaxies.

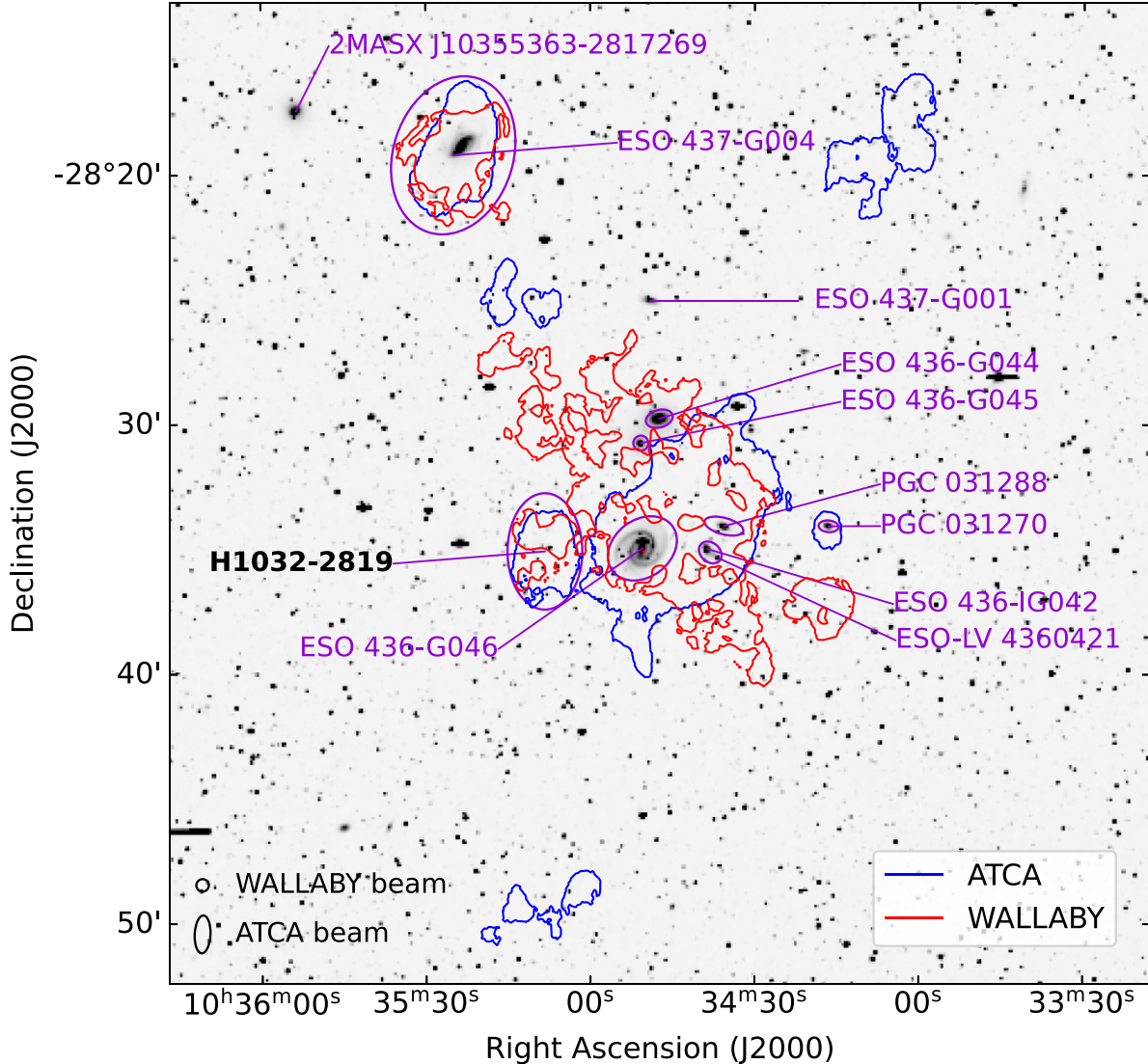


Figure 1. The location of the Klemola 13 galaxies and their optical apertures as defined in Section 4.1 (ellipses) are shown on the g -band Legacy Survey DR10 image. Superposed on this image are the $1 \times 10^{19} \text{cm}^{-2}$ H I column density contour level, representing the boundary of the SoFiA masks. Coordinates, major and minor axes, and position angles are given in Table 3. The tip of the lines point at the centre coordinates from Table 3, except for those of ESO 436-IG042 and ESO-LV 4360421 which point to the respective galaxies. The almost dark cloud (H1032-2819; bold font), is detected in both the ATCA and WALLABY data. The ATCA and WALLABY beams are shown at the bottom left.

The H I spectra for the Klemola 13 system are shown in Fig. 2 for both the SoFiA masked WALLABY and ATCA data. Because the northern galaxy ESO 437 – G004 has a distinct spatial separation from the rest of the system its spectra have been shown separately in orange and light blue. The WALLABY spectra have been smoothed to the same velocity resolution as the ATCA data (20 km s^{-1}) for comparison. It can be seen that the WALLABY and ATCA spectra span roughly the same width and there are some discrepancies. The spectrum that we measure from HIPASS data are also shown. This spectrum was measured using the MBSPECT task in MIRIAD, integrating over a 20 arcmin box centred on RA = 10:35:49 and Dec. = $-28:31:51$, sufficient to contain the intragroup gas seen in ATCA and WALLABY data and all of the galaxies except ESO 437 – G004. The HIPASS data have a velocity resolution of 13.4 km s^{-1} and a 15.5 arcmin beam. However, HIPASS cubes are optimized for point sources, and spatial filtering of extended sources may result

in the loss of flux (Barnes et al. 2001; Meyer et al. 2004). We measure the integrated flux of the HIPASS spectrum to be $16.0 \text{ Jy km s}^{-1}$.

Fig. 3 shows the Legacy Survey DR10 grz images with H I column density contours from WALLABY and ATCA overlaid. The lowest contour levels in Figs 1 and 3 represent the emission at the edge of the SoFiA masks. The densest H I regions line up well in the WALLABY and ATCA observations. In both Figs 3(a) and (b), it can be seen that the highest density H I is around PGC 031288, ESO-LV 4360421 and ESO 436 – IG042, with a peak flux of $0.042/0.015 \text{ Jy km s}^{-1}$ (WALLABY/ATCA) in the latter. The low column density contours can be seen stretching towards the northern galaxy, ESO 437 – G004. WALLABY detects a higher column density of H I in the almost dark cloud H1032 – 2819, while ATCA detects more of its extended emission. This is likely due to excellent coverage of short baselines in the ATCA observations and WALLABY’s flux deficit issue that faint sources are prone to (see section 6 in Westmeier et al. 2022).

Table 3. Key parameters for the interacting system Klemola 13 and its different components. From top to bottom the rows are: right ascension, declination, optical velocity, position angle, major diameter, minor diameter, stellar mass, sSFR, integrated flux, H I mass, H I velocity (v_z), velocity width, rotational velocity, dynamical mass, H I to stellar mass ratio, H I to dynamical mass ratio, stellar to dynamical mass ratio, and the rms centred at the source (only ATCA).

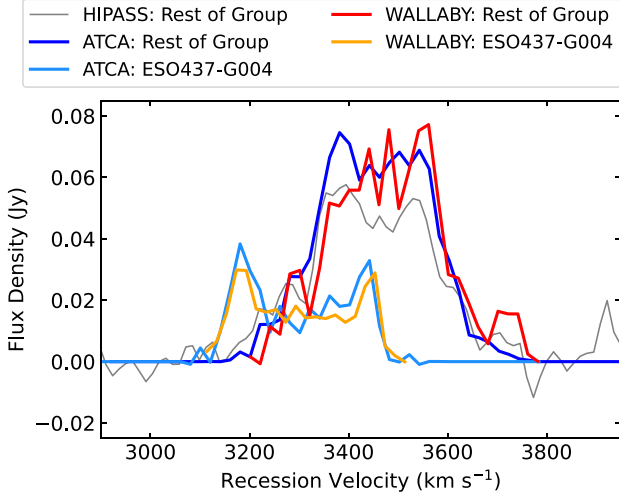
	HI1032 – 2819		ESO 436 – G046		ESO 436 – IG042 + LV4360421		PGC 031 288		PGC 031 270		ESO 436 – G044		ESO 436 – G045		ESO 437 – G004	
RA (J2000)	158.785°	158.711°	158.659°	158.648°	158.569°	158.569°	158.569°	158.569°	158.700°	158.710°	158.710°	158.854°	158.854°	158.854°	158.854°	158.854°
Dec. (J2000)	–28.585°	–28.583°	–28.586°	–28.568°	–28.568°	–28.568°	–28.568°	–28.568°	–28.500°	–28.510°	–28.510°	–28.320°	–28.320°	–28.320°	–28.320°	–28.320°
v_{opt} (km s ^{–1})	–	3390 ± 45	3445 ± 45	3542 ± 45	3570 ± 45	3570 ± 45	3570 ± 45	3570 ± 45	3165 ± 17	3402 ± 17	3402 ± 17	3318 ± 45	3318 ± 45	3318 ± 45	3318 ± 45	3318 ± 45
PA	0°	127°	49°	75°	85°	85°	85°	85°	105°	0°	0°	162°	162°	162°	162°	162°
D_{maj}	280 arcsec	180 arcsec	96 arcsec	76 arcsec	48 arcsec	48 arcsec	48 arcsec	48 arcsec	66 arcsec	36 arcsec	36 arcsec	388 arcsec	388 arcsec	388 arcsec	388 arcsec	388 arcsec
D_{min}	180 arcsec	138 arcsec	46 arcsec	40 arcsec	28 arcsec	28 arcsec	28 arcsec	28 arcsec	42 arcsec	36 arcsec	36 arcsec	288 arcsec	288 arcsec	288 arcsec	288 arcsec	288 arcsec
$\log(M_*/M_\odot)$	8.0 ± 0.7	9.8 ± 0.1	9.4 ± 0.1	9.8 ± 0.1	9.1 ± 0.1	9.1 ± 0.1	9.1 ± 0.1	9.1 ± 0.1	10.2 ± 0.1	9.9 ± 0.1	9.9 ± 0.1	9.7 ± 0.1	9.7 ± 0.1	9.7 ± 0.1	9.7 ± 0.1	9.7 ± 0.1
$\log(\text{sSFR}/\text{yr}^{-1})$	<–9.6	–9.6 ± 0.2	–9.1 ± 0.2	–12.7 ± 0.2	–10.0 ± 0.2	–10.0 ± 0.2	–10.0 ± 0.2	–10.0 ± 0.2	–11.9 ± 0.2	–12.0 ± 0.2	–12.0 ± 0.2	–10.0 ± 0.2	–10.0 ± 0.2	–10.0 ± 0.2	–10.0 ± 0.2	–10.0 ± 0.2
S (Jy km s ^{–1})	1.37 ± 0.14	3.72 ± 0.21	1.99 ± 0.06	1.20 ± 0.09	<0.29	<0.29	<0.29	<0.29	0.71 ± 0.08	0.41 ± 0.05	0.41 ± 0.05	7.23 ± 0.29	7.23 ± 0.29	7.23 ± 0.29	7.23 ± 0.29	7.23 ± 0.29
$\log(M_{\text{HI}}/M_\odot)$	8.86 ± 0.04	9.3 ± 0.02	9.03 ± 0.01	8.81 ± 0.03	–	–	–	–	8.58 ± 0.05	8.34 ± 0.05	8.34 ± 0.05	9.59 ± 0.02	9.59 ± 0.02	9.59 ± 0.02	9.59 ± 0.02	9.59 ± 0.02
v_c (km s ^{–1})	3286 ± 10	3515 ± 20	3473 ± 10	3441 ± 10	–	–	–	–	3555 ± 20	–	–	3276 ± 10	3276 ± 10	3276 ± 10	3276 ± 10	3276 ± 10
w_{50} (km s ^{–1})	47 ± 20	226 ± 20	237 ± 20	183 ± 20	–	–	–	–	216 ± 40	–	–	307 ± 20	307 ± 20	307 ± 20	307 ± 20	307 ± 20
v_{rot} (km s ^{–1})	–	155 ± 30	–	–	–	–	–	–	–	–	–	118 ± 20	118 ± 20	118 ± 20	118 ± 20	118 ± 20
$\log(M_{\text{Dyn}}/M_\odot)$	10.1 ± 0.4	11.0 ± 0.1	11.0 ± 0.1	10.6 ± 0.1	–	–	–	–	10.8 ± 0.1	–	–	10.8 ± 0.1	10.8 ± 0.1	10.8 ± 0.1	10.8 ± 0.1	10.8 ± 0.1
$\log(M_{\text{HI}}/M_*)$	0.9 ± 0.3	–0.5 ± 0.1	–0.5 ± 0.1	–1.0 ± 0.1	–	–	–	–	–1.6 ± 0.1	–1.5 ± 0.1	–1.5 ± 0.1	–0.1 ± 0.1	–0.1 ± 0.1	–0.1 ± 0.1	–0.1 ± 0.1	–0.1 ± 0.1
$\log(M_{\text{HI}}/M_{\text{Dyn}})$	–1.2 ± 0.4	–1.7 ± 0.1	–2.0 ± 0.1	–1.8 ± 0.1	–	–	–	–	–2.2 ± 0.1	–	–	–1.2 ± 0.1	–1.2 ± 0.1	–1.2 ± 0.1	–1.2 ± 0.1	–1.2 ± 0.1
$\log(M_*/M_{\text{Dyn}})$	–2.1 ± 1.7	–1.2 ± 0.2	–1.4 ± 0.2	–0.7 ± 0.2	–	–	–	–	–0.6 ± 0.2	–	–	–1.1 ± 0.2	–1.1 ± 0.2	–1.1 ± 0.2	–1.1 ± 0.2	–1.1 ± 0.2
S (Jy km s ^{–1})	0.92 ± 0.13	4.32 ± 0.18	1.01 ± 0.04	1.16 ± 0.06	0.06 ± 0.02	0.06 ± 0.02	0.06 ± 0.02	0.06 ± 0.02	<0.27	<0.18	<0.18	6.72 ± 0.45	6.72 ± 0.45	6.72 ± 0.45	6.72 ± 0.45	6.72 ± 0.45
$\log(M_{\text{HI}}/M_\odot)$	8.69 ± 0.06	9.36 ± 0.02	8.73 ± 0.02	8.79 ± 0.02	7.52 ± 0.13	7.52 ± 0.13	7.52 ± 0.13	7.52 ± 0.13	–	–	–	9.55 ± 0.03	9.55 ± 0.03	9.55 ± 0.03	9.55 ± 0.03	9.55 ± 0.03
v_c (km s ^{–1})	3266 ± 10	3421 ± 10	3448 ± 10	3429 ± 10	3540 ± 10	3540 ± 10	3540 ± 10	3540 ± 10	–	–	–	3237 ± 10	3237 ± 10	3237 ± 10	3237 ± 10	3237 ± 10
w_{50} (km s ^{–1})	57 ± 20	238 ± 20	227 ± 20	179 ± 20	109 ± 20	109 ± 20	109 ± 20	109 ± 20	–	–	–	291 ± 20	291 ± 20	291 ± 20	291 ± 20	291 ± 20
v_{rot} (km s ^{–1})	–	142 ± 30	–	–	–	–	–	–	–	–	–	116 ± 20	116 ± 20	116 ± 20	116 ± 20	116 ± 20
$\log(M_{\text{Dyn}}/M_\odot)$	10.2 ± 0.3	11.0 ± 0.2	10.9 ± 0.1	10.5 ± 0.1	10.0 ± 0.1	10.0 ± 0.1	10.0 ± 0.1	10.0 ± 0.1	–	–	–	10.8 ± 0.1	10.8 ± 0.1	10.8 ± 0.1	10.8 ± 0.1	10.8 ± 0.1
$\log(M_{\text{HI}}/M_*)$	0.7 ± 0.3	–0.4 ± 0.1	–0.8 ± 0.1	–1.0 ± 0.1	–1.6 ± 0.2	–1.6 ± 0.2	–1.6 ± 0.2	–1.6 ± 0.2	–	–	–	–0.1 ± 0.1	–0.1 ± 0.1	–0.1 ± 0.1	–0.1 ± 0.1	–0.1 ± 0.1
$\log(M_{\text{HI}}/M_{\text{Dyn}})$	–1.5 ± 0.3	–1.6 ± 0.2	–2.2 ± 0.1	–1.8 ± 0.1	–2.4 ± 0.3	–2.4 ± 0.3	–2.4 ± 0.3	–2.4 ± 0.3	–	–	–	–1.2 ± 0.1	–1.2 ± 0.1	–1.2 ± 0.1	–1.2 ± 0.1	–1.2 ± 0.1
$\log(M_*/M_{\text{Dyn}})$	–2.3 ± 1.1	–1.2 ± 0.2	–1.4 ± 0.2	–0.7 ± 0.2	–0.8 ± 0.2	–0.8 ± 0.2	–0.8 ± 0.2	–0.8 ± 0.2	–	–	–	–1.1 ± 0.2	–1.1 ± 0.2	–1.1 ± 0.2	–1.1 ± 0.2	–1.1 ± 0.2
rms (mJy beam ^{–1})	0.85	0.80	0.76	0.77	0.75	0.75	0.75	0.75	0.82	0.80	0.80	1.95	1.95	1.95	1.95	1.95

WALLABY

ATCA

Table 4. Flux and H I mass of the entire interacting system compared to that of the intragroup gas outside of the galaxy apertures.

		Entire system	Intragroup gas
WALLABY	S (Jy km s ⁻¹)	27.98 ± 0.72	11.35 ± 0.88
	$\log(M_{\text{HI}}/M_{\odot})$	10.17 ± 0.01	9.78 ± 0.03
ATCA	S (Jy km s ⁻¹)	27.07 ± 0.51	12.87 ± 0.81
	$\log(M_{\text{HI}}/M_{\odot})$	10.16 ± 0.01	9.84 ± 0.03

**Figure 2.** A comparison of the H I spectra for ESO 437 – G004 and the rest of the Klemola 13 system for the ATCA, WALLABY, and HIPASS data.

4.2 Comparison with the literature

The masks differ significantly between the public release WALLABY data (Westmeier et al. 2022) and the version presented here. Re-running SoFiA with parameters specific to this source rather than relying on the automated pipeline allows us to recover more extended emission. The automated pipeline is good for general WALLABY detections, however in diffuse, interacting regions such as this, varying the SoFiA parameters can allow for a more comprehensive analysis, as shown in Batten et al. (in preparation). Fig. 4 shows the outline of the flattened masks of both WALLABY data sets overlaid onto the ATCA column density image. Only the published WALLABY SoFiA run identifies H1032 – 2819 as a separate source distinct from the rest of Klemola 13. The WALLABY mask created for this paper suggests a bridge, which was not identified by McMahon (1993) or Duc et al. (1999). Nevertheless, the velocity fields in Fig. 5 do show a discontinuity, implying that H1032 – 2819 is more probably a distinct source, that is seen in projection, rather than a simple easterly extension from ESO 436 – G046.

To compare our measured properties of H1032 – 2819 with the previous detections, the published values of flux, central velocity, and velocity width are shown in Table 5. The VLA data are from McMahon (1993), and the Nançay data are from Duc et al. (1999). The WALLABY measurement using the mask defined in this paper has recovered the most flux. All of the central velocities lie within ~ 50 km s⁻¹ of each other.

In both of the previous studies containing H1032 – 2819 (McMahon 1993; Duc et al. 1999), this source is identified as an H I cloud without an optical counterpart. However, using the most recent Legacy Survey DR10, for the first time an extremely faint

optical counterpart is visible by eye. Section 4.3 explores the optical properties we have derived for this almost dark cloud.

4.3 Stellar mass and specific star formation rate

The stellar masses for all the galaxies except H1032 – 2819 were estimated from the *Wide-field Infrared Survey Explorer* (WISE, Wright et al. 2010). This is done using the WISE W1 and W2 magnitudes, as shown in equations (1) and (2) (Jarrett et al. 2023):

$$\log\left(\frac{\Upsilon_*^{3.4\mu\text{m}}}{M_{\odot}/L_{\odot}}\right) = -0.376 - 1.053 \times (W1 - W2), \quad (1)$$

$$\frac{L_{3.4\mu\text{m}}}{L_{\odot}} = 10^{-0.4(M - M_{\text{SUN}})}, \quad (2)$$

where $\Upsilon_*^{3.4\mu\text{m}}$ is the stellar mass to light ratio in the W1 band, $L_{3.4\mu\text{m}}$ is the luminosity in the W1 band, M is the absolute magnitude of the source in the W1 band, and M_{SUN} is the absolute magnitude of the sun in the W1 band ($M_{\text{SUN}} = 3.24$ mag; Jarrett et al. 2013). The scatter in equation (1) is 0.11 dex. The stellar mass of ESO 436 – IG042 and ESO – LV 4 360 421 are summed in Table 3.

H1032 – 2819 was not detected by WISE and thus the WISE W1 and W2 magnitudes were not available, so the stellar mass is derived from the Legacy Survey DR10 images. The apparent magnitude and average surface brightness measured in an elliptical aperture containing all the visible emission for each of the bands available (g, r, i, z) for H1032 – 2819 are given in Table 6. In making this measurement we masked out the significant foreground stars and removed the sky background. Using the g and r bands, we estimated the stellar mass using the results of Du et al. (2020), which specifically relates to the $g - r$ colour of low surface brightness galaxies. We estimate a stellar mass of $\log(M_*/M_{\odot}) = 7.98$ and a stellar mass to light ratio of $\Upsilon_* = 1 M_{\odot}/L_{\odot}$. For comparison, we also calculated the stellar mass using the relation determined by Robotham et al. (2020), which uses the spectral energy distribution of ProSpect. This approach gives rise to a higher value of $\log(M_*/M_{\odot}) = 8.35$.

To perform the structural analysis of the object we additionally performed a fit to a Sérsic model using the IMFIT software (Erwin 2015). For this we performed a masking of all sources external to the object, using a combination of the masking provided using SEXTRACTOR (Bertin & Arnouts 1996) and manual masks. First, we use a sum image of the g and r bands (the deepest ones) to obtain values for position, position angle ($33.8^{\circ} \pm 1.5^{\circ}$) and ellipticity (0.42 ± 0.02), which are subsequently fixed in the individual g, r, i , and z band fitting, providing the rest of the following parameters: Sérsic index $n = 0.89 \pm 0.06$, effective radius $r_{\text{eff}} = 26.9$ arcsec ± 0.8 arcsec (6 kpc), and central g -band surface brightness $\mu_{\text{cent}, g} = 26.3 \pm 0.3$ mag arcsec⁻².

The specific star formation rate (sSFR) was calculated using the method outlined in Janowiecki et al. (2017) and Reynolds et al. (2022). This method is summarized in equations (3)–(6):

$$\text{sSFR} = (\text{SFR}_{\text{NUV}} + \text{SFR}_{\text{MIR}})/M_*, \quad (3)$$

$$\text{SFR}_{\text{NUV}}/(M_{\odot}\text{yr}^{-1}) = 10^{-28.165} L_{\text{NUV}}/(\text{erg Hz}), \quad (4)$$

$$\text{SFR}_{\text{W3}}/(M_{\odot}\text{yr}^{-1}) = 4.91 \times 10^{-10} (L_{\text{W3}} - 0.201L_{\text{W1}})/L_{\odot}, \quad (5)$$

$$\text{SFR}_{\text{W4}}/(M_{\odot}\text{yr}^{-1}) = 7.50 \times 10^{-10} (L_{\text{W4}} - 0.044L_{\text{W1}})/L_{\odot}, \quad (6)$$

where SFR_{NUV} is the near-ultraviolet star formation rate derived from L_{NUV} , the GALEX NUV-band luminosity (Martin et al. 2005). SFR_{MIR}

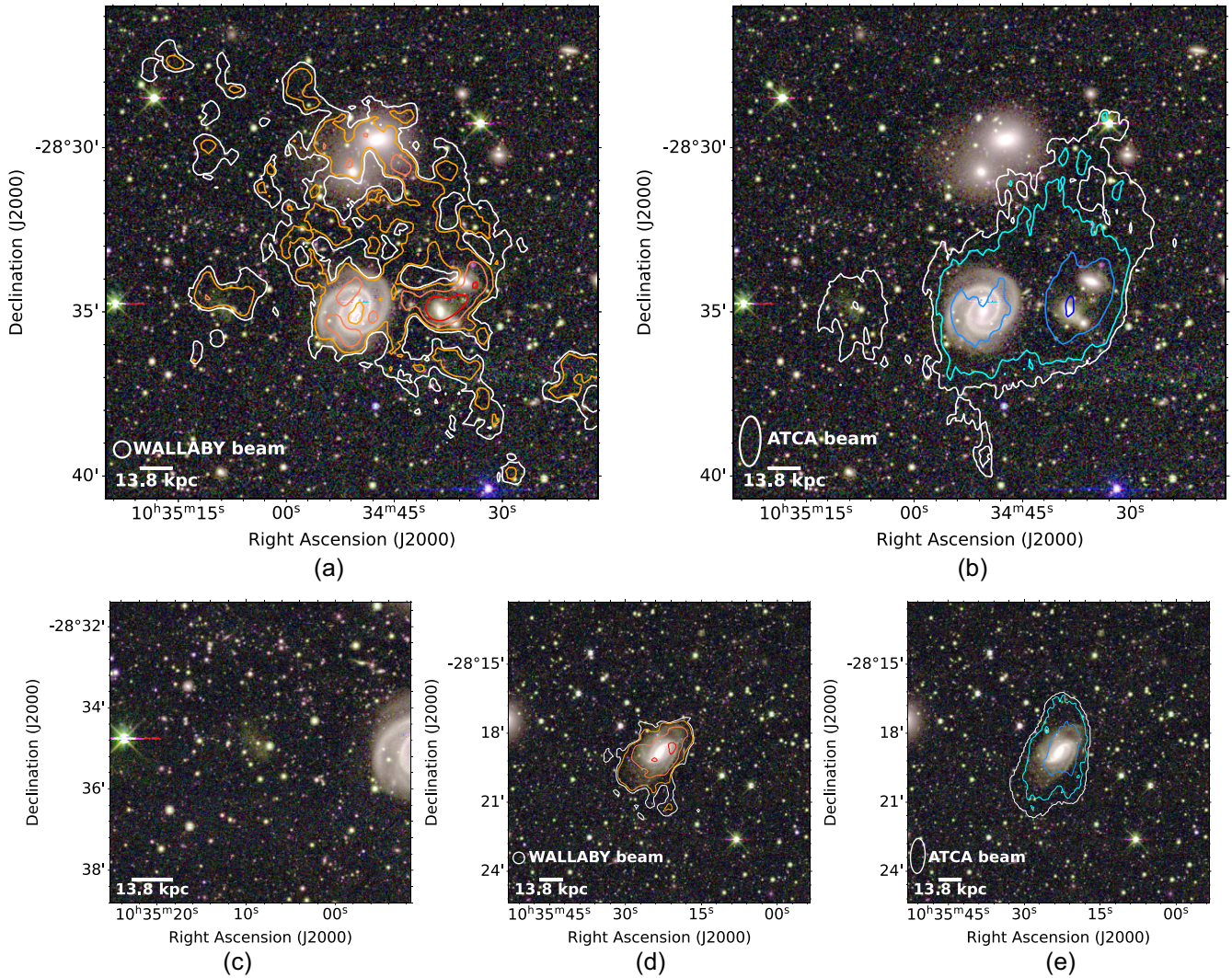


Figure 3. Legacy Survey DR10 *grz* images overlaid with H I contours. The contour levels are 1×10^{19} , 1×10^{20} , 3×10^{20} , and $7 \times 10^{20} \text{ cm}^{-2}$. (a) WALLABY contours over central region of the group. (b) ATCA contours over the central region of the group. (c) The Legacy Survey image centred on the almost dark cloud. (d) The WALLABY contours over ESO 347 – G004. (e) ATCA contours over ESO 437 – G004.

is the mid-infrared star formation rate derived L_{W4} (or L_{W3} if the galaxy was undetected in $W4$) with a correction from L_{W1} to remove the contributions of old stars, where L_{W1} , L_{W3} , and L_{W4} *WISE* $W1$ -, $W3$ -, and $W4$ -band luminosities. If this correction was larger than the $W3$ or $W4$ luminosity contributions, then the MIR contribution to the total SFR is assumed to be zero (this is the case for PGC 031288, ESO 436 – G044 and ESO 436 – G045). This method of calculating the mid-infrared SFR was chosen by Janowiecki et al. (2017) to enable comparison with the extended *GALEX* Arcibo SDSS Survey (xGASS, Catinella et al. 2018), which we also show in Section 5.1. Reynolds et al. (2022) found that for the Hydra Cluster, their SFR values had error ≤ 0.1 dex using this method, so an uncertainty of 0.1 dex was assumed for our SFR values. The SFR for ESO 346 – IG042 and ESO-LV 4360421 are summed in Table 3. H1032 – 2819 was not detected in *WISE* or *GALEX*, so a 3σ upper limit to the SFR was estimated from the *GALEX* NUV image using the H I aperture. All of the derived stellar masses and sSFRs are presented in Table 3, and the quantities used to calculate them are presented in Table B1.

4.4 Kinematic analysis

The velocity field for H1032 – 2819 can be seen in the moment 1 images in Fig. 5. The mean velocity is similar to that of ESO 437 – G004, but about 270 km s^{-1} lower than the more nearby ESO 436 – G046. However, although the velocity width is $w_{50} = 47 \text{ km s}^{-1}$, it appears that H1032 – 2819 is not a regularly rotating disc. Common features between the WALLABY and ATCA velocity fields are that it is slightly more blueshifted to the west (towards ESO 436 – G046), and slightly more redshifted in the south.

The dynamical masses of all galaxies except ESO 436 – G046 and ESO 437 – G004 have been estimated using $M = rv^2/G$, where v is half of the w_{50} value, r is the average of the semi-major and minor axes of the aperture, and G is the gravitational constant. Sources with inclinations greater than 30° have their v value corrected for inclination by a factor of $1/\sin(i)$, where i is the inclination calculated from the ratio of the major and minor axes of the optical apertures. Using this method, the dynamical mass of H1032 – 2819 is estimated to be $1 \times 10^{10} M_\odot$ using an inclination of 50° . As this mass is $\sim 15 \times$ larger than the sum of the H I and stellar mass, it is possible that

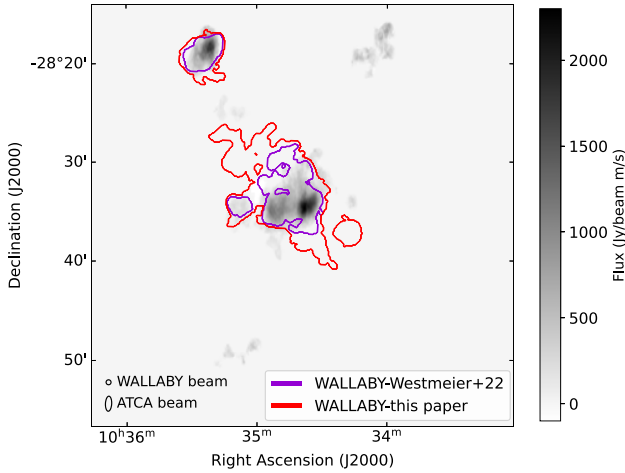


Figure 4. The 2D mask outlines of both WALLABY data sets overlaid on the ATCA column density image. The sources published in Westmeier et al. 2022 are WALLABY J103508 – 283427, WALLABY J103523 – 281855, and WALLABY J103442 – 283406.

H1032 – 2819 contains dark matter. However this is unlikely, as this estimate relies on the cloud being self-gravitating in hydrostatic equilibrium. It is much more likely that tidal and ram pressure forces have contributed to a high mass estimate by stretching the source and adding velocity perturbations.

The more massive galaxies, ESO 437 – G004 and ESO 436 – G046, appear to be regular rotators, so 3DBAROLO (Di Teodoro & Fraternali 2015) was used to model their kinematics. 3DBAROLO fits 3D tilted ring models to the H I emission in the data cubes, resulting in the velocity fields and rotation curves shown in Figs A1 and A2. For ESO 436 – G046, the aperture shown in Fig. 1 was applied to the SoFiA masked cube. For ESO 437 – G004, we used the SoFiA mask that included its entire H I content but only modelled out to a radius of ~ 20 kpc, which excludes the outer regions as they are more affected by noise. 3DBAROLO was set to fit for three free parameters: rotation velocity (V_{rot}), inclination (i) and position angle (ϕ), as shown in Figs A1(b) and A2(b). We oversample the number of rings, fitting roughly two rings per beam, as done in the WALLABY kinematic modelling pipeline (Deg et al. 2022) and in previous WALLABY studies (Elagali et al. 2019; Reynolds et al. 2019). The rotation velocities and dynamical masses derived from these models have been included in Table 3, where the error in the dynamical mass is derived from the error in the rotation velocity. The optical coordinates from Table 3 were used as the centre, and a dispersion velocity of 11 km s^{-1} was assumed, as typically found in massive and dwarf disc galaxies (e.g. Iorio et al. 2017; Bacchini et al. 2019; Mancera Piña et al. 2021). To estimate the rotation velocities for ESO 4363 – G046 and ESO 437 – G004, the last 5 (4) and 4 (4) points in the WALLABY (ATCA) rotation curves were averaged, respectively. Similar results for ESO 437 – G004 were produced using both the ATCA and WALLABY data, which is a testament to the reliability of the fits. Meaningful models could not be created for all of the components of the system. The 3DBAROLO model for ESO 436 – G046 is not reliable, as can be seen in the residuals in Fig. A2(a), as it is not a perfectly regularly rotating disc. Nevertheless, we have included the rotation velocity derived from this model in Table 3 so that comparisons can be made. The kinematic models are quite sensitive to the initial input parameters, and smoothing over

small-scale structure can lead to improved residuals by a factor of ~ 3 as described in Appendix A.

Only ESO 437 – G004 has a kinematic model in the WALLABY pilot data release 1 (PDR1, Deg et al. 2022). The WALLABY PDR1 kinematic model was created with the WALLABY Kinematic Analysis Proto-Pipeline (WKAPP). The WKAPP WALLABY model has an inclination of 58° , a position angle of 316° , and a rotation velocity of 163 km s^{-1} , which is higher than the values obtained here. WKAPP combines 3DBAROLO and FAT (Kamphuis et al. 2015) results, and does not allow the position angle and inclination to vary between the rings (as they do in our models). Although both produced rotation velocities higher than our models, the FAT rotation velocity was significantly larger than that of 3DBAROLO. The other significant factor causing the increase in rotation velocity is the mask. In order to allow FAT and 3DBAROLO run as similarly as possible, WKAPP creates its own masks. In contrast, we use the SoFiA mask to be consistent with the rest of our analysis. Allowing 3DBAROLO to create its own mask on our data gives higher outer rotation velocities using the ATCA data. For the WALLABY data, the entire rotation curve velocity is increased. However, this caused the overall kinematic model to have much higher residuals.

5 DISCUSSION

5.1 Global galaxy properties

To see how the group environment affects the properties of H1032 – 2819 and the other galaxies in the interacting system, we have plotted them against galaxies from xGASS for common scaling relations in Fig. 6. The WALLABY detections in the Eridanus supergroup (For et al. 2021) and the WALLABY detections in the Hydra field (Reynolds et al. 2022) are also plotted for comparison. HUDs from Leisman et al. (2017) and Mancera Piña et al. (2020) have been included in orange. The stellar mass against H I mass is plotted in Fig. 6(a) and the H I gas fraction against stellar mass is plotted in Fig. 6(b). It is clear that H1032 – 2819 has a significantly lower stellar mass than all of the xGASS galaxies. Only two galaxies lie above the median (ESO 436 – G046 and ESO 437 – G004). The three galaxies that appear extremely H I deficient, ESO 436 – G044, ESO 436 – G045, and PGC 031270, have H I masses below even that of scatter of the xGASS galaxies. Interestingly, adding the H I mass of the almost dark cloud (H1032 – 2819) to the closer galaxies (ESO 436 – G044 and ESO 436 – G045) brings them up into the scatter of the xGASS galaxies, as shown by the cross markers in Fig. 6(a). Hence, in general, the galaxies in this system tend to be H I deficient. There are two explanations for this. First, we are measuring the H I gas within the apertures defined by each galaxy’s optical radius, however it is common for galaxies to have H I gas extending past twice the optical radius. If the apertures of these galaxies are extended to twice the optical radii, PGC 031 270 still has an H I mass well below the scatter of the xGASS sample ($M_{\text{HI}} = 6.9 \times 10^7 M_\odot$), but the H I masses of ESO 436 – G044 and ESO 436 – G045 are brought up just inside the scatter ($M_{\text{HI}} = 8.0 \times 10^8$ and $3.7 \times 10^8 M_\odot$, respectively). Secondly, the galaxies tend to be H I deficient as the group environment has caused gas to be stripped from the individual galaxies and become shared between the components of the group.

The stellar mass against sSFR is shown in Fig. 6(c) and the sSFR against gas fraction is shown in Fig. 6(d). PGC 031 288 has a lower sSFR than all the galaxies, apart from two xGASS sources. ESO 436 – G046 is the only Klemola 13 galaxy with an sSFR above the

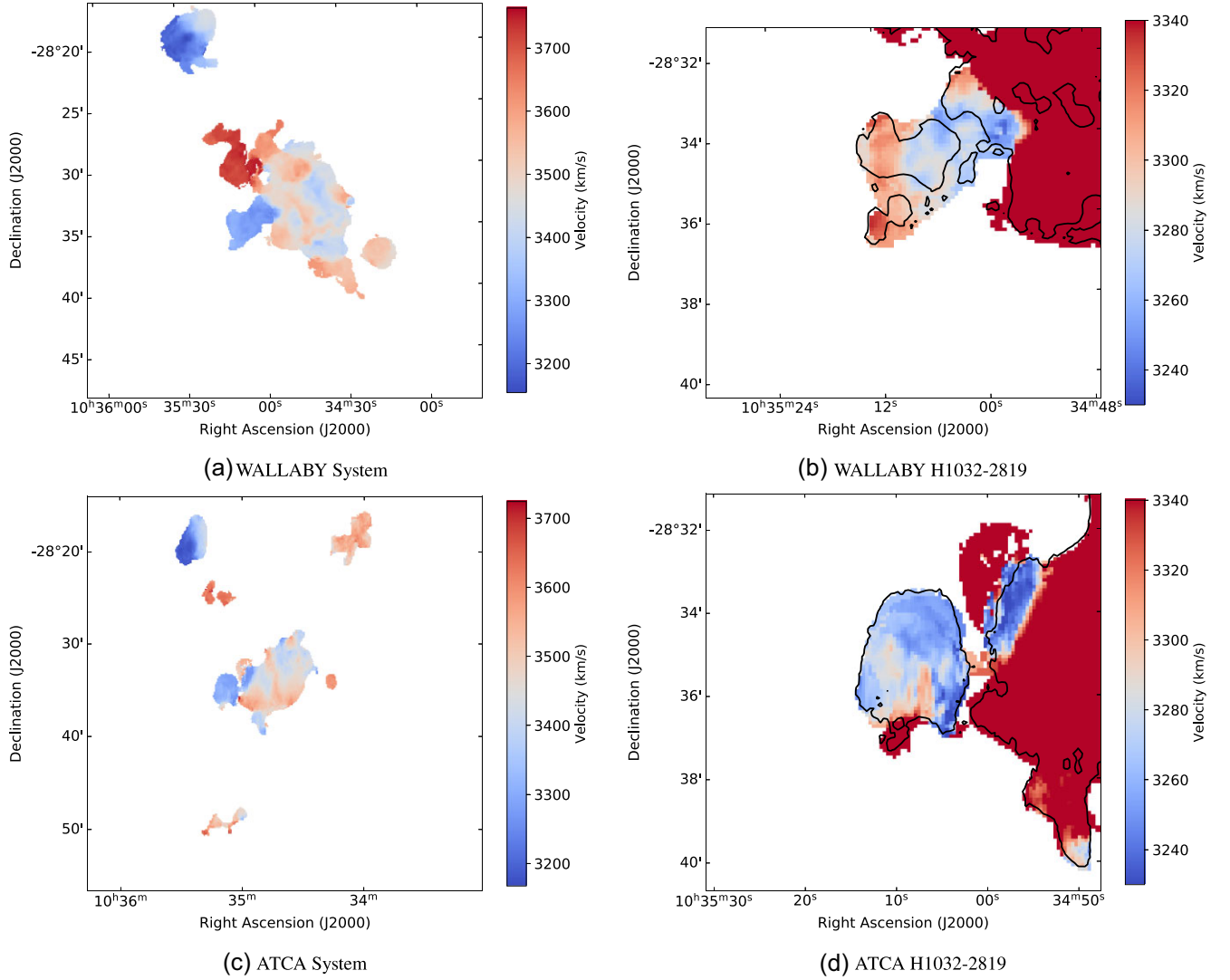


Figure 5. The H I velocity fields from WALLABY (top row) and ATCA (bottom row). The left column is for the whole Klemola 13 system; the right column is zoomed-in on the almost dark cloud H1032 – 2819. The black contour shows the $1 \times 10^{19} \text{cm}^{-2}$ column density level for the respective data sets.

Table 5. Comparison of the almost dark cloud with the literature. Uncertainties are included if given in the literature. Width refers to w_{50} except * which indicates the width used in McMahon (1993) which is roughly equivalent to w_{20} .

	S (Jy km s $^{-1}$)	v_c (km s $^{-1}$)	Width (km s $^{-1}$)
ATCA	0.92 ± 0.11	3266 ± 10	57 ± 20
WALLABY – this paper	1.37 ± 0.14	3255 ± 2	46 ± 4
WALLABY – Westmeier + 22	0.70 ± 0.09	3295	135
Nançay	0.96	3280	95
VLA	0.44 ± 0.10	3304	$\leq 42^*$

Table 6. Optical properties of H1032 – 2819. The properties from top to bottom are apparent AB magnitude and mean surface brightness.

Property	g band	r band	i band	z band
m_{AB} (mag)	18.6 ± 0.3	18.1 ± 0.2	17.5 ± 0.2	17.9 ± 0.3
μ (mag arcsec $^{-2}$)	27.0 ± 0.3	26.4 ± 0.2	25.9 ± 0.2	26.3 ± 0.3

median for its stellar mass. H1032 – 2819 has a higher gas fraction than all the xGASS galaxies. The sSFR of H1032 – 2819 also sits at the high end of the range spanned by the xGASS galaxies, but for its given gas fraction, its sSFR is low. This is in line with the conclusions of Kado-Fong et al. (2022), who find that UDGs tend to have low SFR as they are less efficient at converting H I to molecular gas and to stars.

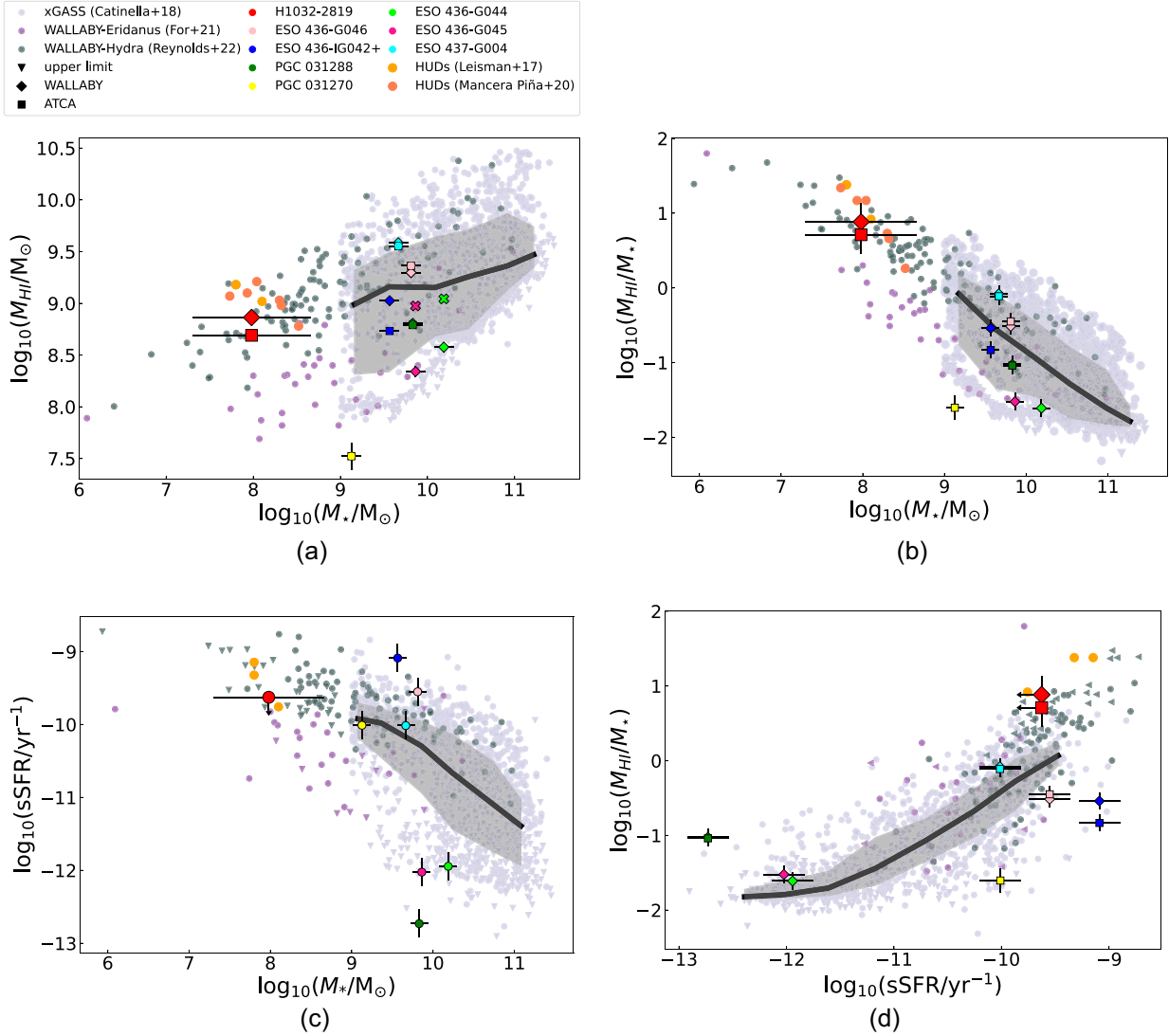


Figure 6. Scaling relations for the galaxies in Klemola 13 compared with xGASS, the WALLABY detections in the Hydra field, and the WALLABY detections in the Eridanus supergroup. Additionally, HUDs have been included. The solid line indicates the rolling median (with bin widths of 0.45) and the shaded region shows the interquartile region of the xGASS detections and non-detections. The almost dark cloud (H1032 – 2819) has a larger marker for emphasis. The quantities derived for the sources in Klemola 13 can be found in Table 3. In the legend, ESO 436 – IG042 + refers to the aperture containing both ESO 436 – IG042 and ESO-LV 4360421. (a) H I mass against stellar mass. The cross symbols indicate that the H I mass of the almost dark cloud has been added to the galaxy. (b) Gas fraction against stellar mass. (c) Stellar mass against sSFR. (d) Gas fraction against sSFR.

5.2 Origin and evolution of the Almost dark cloud

5.2.1 Origin

Due to the proximity of H1032 – 2819 to the other galaxies in Klemola 13 and its location near the Hydra Cluster, it appears unlikely that this almost dark cloud has a primordial origin. As discussed in Section 4.4, the cloud does not appear to be self-gravitating. However, there is insufficient data to definitively rule out a primordial origin, and there are no obvious tidal features in the optical.

Instead, the cloud’s origin and evolution is likely to be dominated by interactions. Uncovering the orbital history of each component of this system will not be possible given the observations available and the complexity of the system. Nevertheless we have devised two tidal fly-by interaction scenarios to give some insight into the likely formation mechanism of the almost dark cloud. In this case, in a tidal

fly-by interaction the motion of the northern galaxy past the rest of the group causes gas to be stripped and form the cloud.

The first scenario considers that the almost dark cloud is the result of a fly-by interaction between the northern galaxy, ESO 437 – G004, and one or both of the nearby extremely H I deficient galaxies ESO 436 – G044 and ESO 436 – G045. It was shown previously in Fig. 6(a) that adding the H I mass of H1032 – 2819 to either of these galaxies brings them back up to within the scatter of the xGASS sample. It is also important to note that the H1032 – 2819 and ESO 437 – G004 have similar line-of-sight velocities. In this fly-by scenario, the gas from these less massive galaxies was removed by the tidal force of ESO 437 – G004 and sling shot out of the group, forming the almost dark cloud in the foreground with a smaller recession velocity.

Alternatively, the almost dark cloud could have formed through a tidal fly-by interaction with ESO 436 – G046, the large spiral

galaxy closest to its current position. In this case, the motion of ESO 437 – G004 past ESO 436 – G046, causes the H I cloud to form from tidal stripping. To help quantify this, we calculated the tidal strength parameter, S_{tid} , as given in Wang et al. (2022) for these two galaxies in relation to the cloud at their current positions:

$$S_{\text{tid}} = \frac{M_{\text{gal}}}{M_{\text{cloud}}} \left(\frac{R_{\text{cloud}}}{d_{\text{proj}}} \right)^2 \left(\frac{v_{\text{circ,cloud}}}{\Delta v_{\text{rad}}} \right), \quad (7)$$

where M_{gal} is the dynamical mass estimated using the 3DBAROLO model and M_{cloud} is the sum of the H I and stellar masses of the cloud, R_{cloud} is the average of the major and minor radii of our defined aperture, d_{proj} is the projected distance between the cloud and the galaxy, $v_{\text{circ,cloud}}$ is the circular velocity of the cloud (WALLABY value for self gravitating cloud), and Δv_{rad} is the difference between the line-of-sight velocities for the cloud and the galaxy (WALLABY values used). The projected distances between the cloud and ESO 436 – G046, and the cloud and ESO 437 – G004 are 54 and 202 kpc, respectively. Despite ESO 437 – G004 having a much closer velocity to the cloud, the smaller projected distance of ESO 436 – G046 leads to a tidal strength more than twice as large as that of ESO 437 – G004 ($S_{\text{tid}} = 3.4$ and 1.4 for ESO 436 – G046 and ESO 437 – G004, respectively). Of course, in this fly-by scenario, the formation of the cloud took place when ESO 437 – G004 was much closer. If at some point in its orbital history ESO 437 – G004 was the same distance from the cloud as ESO 436 – G046 is today, ESO 437 – G004 would have had a tidal strength ~ 8 times larger ($S_{\text{tid}} = 28$). This suggestion is supported by the velocity of the cloud being more similar to that of ESO 437 – G004, rather than that of the more nearby galaxies. Using the relation between the half-light radius and the virial radius from Kravtsov (2013), we also found that the dark cloud lies within the virial radii of both ESO 436 – G046 and ESO 437 – G004, making it especially susceptible to tidal forces.

Like the TDGs in Kaviraj et al. (2012), H1032 – 2819 has a stellar mass less than 10 per cent of its parents and lies within 15 optical half-light radii of the parent galaxies. It is also known that TDG do not contain a significant amount of dark matter (e.g. Bournaud & Duc 2006; Lelli et al. 2015; Gray et al. 2023). Although it is possible that H1032 – 2819 may contain dark matter based on the dynamical mass estimation performed in Section 4.4 (which relies on the assumption that it is self-gravitating), a tidal origin is still favoured. When estimating the dynamical masses for their TDGs, Gray et al. (2023) found that including a rough correction for turbulence and asymmetric drift can significantly change the dynamical mass estimates.

H1032 – 2819 appears faint and diffuse, leading us to question whether the almost dark cloud could in fact be an UDG. The criteria defined by van Dokkum et al. (2015) is that an UDG must have an effective radius greater than 1.5 kpc and a central surface brightness fainter than $24 \text{ mag arcsec}^{-2}$. As discussed in Section 4.3, the cloud has an effective radius of 6 kpc and a central g-band surface brightness of $26.3 \pm 0.3 \text{ mag arcsec}^{-2}$. Thus, the cloud does meet the criteria of a UDG, and bears similarities to HUDs (e.g. Leisman et al. 2017; Mancera Piña et al. 2020), which have been included in Fig. 6. UDGs can have a range of formation mechanisms, including tidal interactions, such as the UDGs studied in Jones et al. (2021).

5.2.2 Evolution

Being part of an interacting group, tidal forces can clearly play a dominant role in the origin of the almost dark cloud and in explaining the considerable amount of intragroup gas. But, due to the location

of Klemola 13 just inside the virial radius of the Hydra cluster (see Reynolds et al. 2021), ram pressure will also play an important part in the subsequent evolution of the gaseous components of the system and quenching of star formation in the group members. To quantify this effect, we have used the RPS strength parameter S_{rps} , as defined in Lin et al. (2023) and Wang et al. (2021):

$$S_{\text{rps}} = \frac{P_{\text{ram}}}{F_{\text{anch}}}, \quad (8)$$

$$P_{\text{ram}} = 1.4 m_p n (\Delta v)^2, \quad (9)$$

$$F_{\text{anch}} = 2\pi G (\Sigma_* + \Sigma_{\text{gas}}) \Sigma_{\text{gas}}, \quad (10)$$

where values of S_{rps} greater than 1 indicate a susceptibility to ram pressure stripping. In this definition, P_{ram} is the ram pressure and F_{anch} is the anchoring force. m_p is the proton mass, Δv is the galaxy velocity relative to the cluster medium, estimated using its line-of-sight velocity difference with the mean cluster velocity, G is the gravitational constant, and Σ_* and Σ_{gas} are the stellar and gas surface densities respectively. n is intracluster medium number density at the projected distance from the cluster centre, as defined in Wang et al. (2021). In our calculations we use the Hydra Cluster centre and velocity used in Wang et al. (2021) (RA = 159.0865° , Dec. = -27.5629° and $v = 3686 \text{ km s}^{-1}$). For simplicity, we assume a constant surface density when calculating Σ_* and Σ_{gas} in equation (10). Errors associated with M_* and M_{HI} will result in typical errors in S_{rps} of ~ 28 per cent and are shown in Fig. 7(a). Fig. 7(a) presents S_{rps} as a function of Δv for each component of the system, with the markers representing the estimated values of Δv . Wang et al. (2021) argue that n is an upper limit, and the estimated value of Δv is a lower limit, and that the errors cancel out to some extent. From Fig. 7(a), we can see that the almost dark cloud is prone to RPS regardless of the velocity difference from the cluster centre. Fig. 7(b) shows S_{rps} as a function of radius for ESO 436 – G046 and ESO 437 – G004. We calculate the value of S_{rps} in annuli with width Δr equal to the value used in the respective 3DBAROLO models. For this plot, we include the combined effect of stars, gas and dark matter on the strength of the anchoring force. For Fig. 7(b), we replace equation (10) with equation (11) to calculate the anchoring force:

$$F_{\text{anch}} = 2\pi G \Sigma_{\text{dyn}} \Sigma_{\text{gas}}, \quad (11)$$

where the rotation velocity and the gas surface density from 3DBAROLO at the given radius are used to calculate Σ_{dyn} and Σ_{gas} , respectively. For details on the uncertainties associated with the 3DBAROLO models, see Section 4.4 and Appendix A. The dotted lines in Fig. 7(b) extrapolate the trend beyond the radius of the 3DBAROLO models assuming a flat rotation curve (using the rotation velocity given in Table 3) and a constant gas density equal to that of the outer radius of the model. This serves as an upper limit to S_{rps} as the outer radii beyond the model would have even lower gas surface densities. This figure highlights that the gas that remains today is tightly held, but extended gas that may have been associated to the galaxies in the past would have been susceptible to RPS.

5.3 Comparisons with other H I clouds

Klemola 13 has some similarities to other well-studied groups. Dark and almost dark clouds have been found to be rare by previous studies as they are difficult to identify in large numbers due to the relative surface brightness sensitivity limits in both the large H I and the large optical surveys. By combining Parkes and ATCA observations

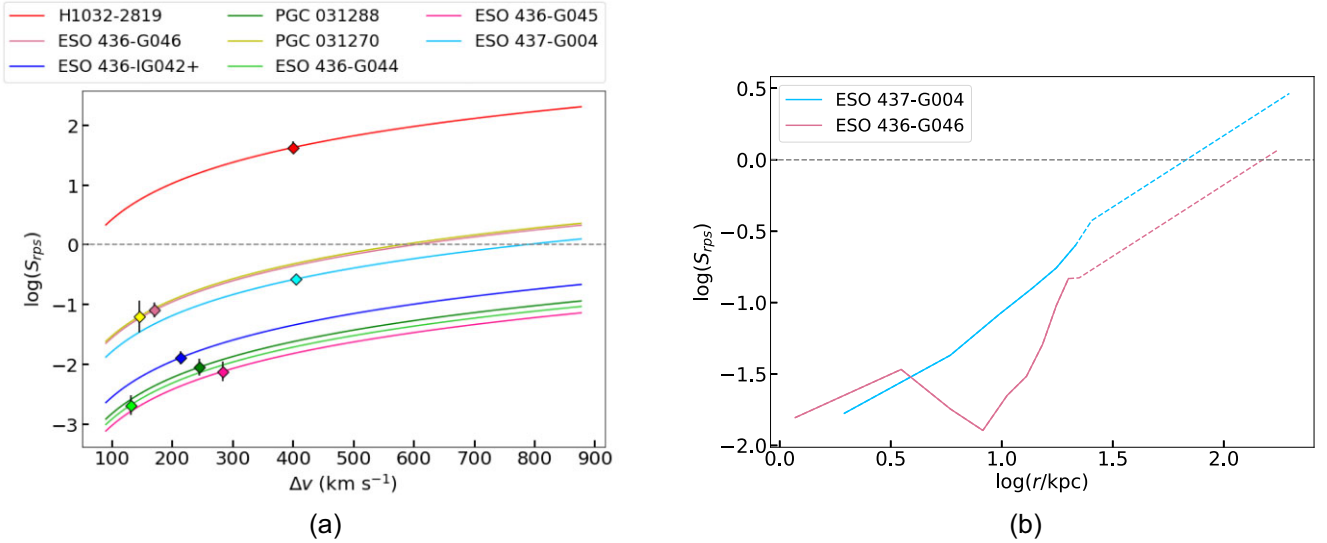


Figure 7. The ram pressure strength parameter (defined in equations 8–11) as a function of velocity difference from the (left; a) cluster centre and (right; b) radius. Ram pressure becomes significant above the horizontal line at $S_{\text{rps}} = 1$.

of the NGC 3783 group, Kilborn et al. (2006) found one detection, GEMS.N3783_2, that did not have an optical counterpart in the NASA/IPAC Extragalactic Database (NED) or 6dFGS. It has an HI mass of $4 \times 10^8 M_{\odot}$, comparable to the $7 \times 10^8 M_{\odot}$ almost dark cloud in Klemola 13. Similarly, they find that their dark cloud is most likely to be the result of a tidal interaction between the nearby gas-rich spiral (ESO 378 – G003) and one or more galaxies in the group. This is evident from the proximity of ESO 378 – G003 to the dark cloud (a projected distance of 450 kpc) and its irregular HI and velocity distribution on one side of the galaxy. Alternatively, they suggest that the dark cloud could be an extremely low surface brightness galaxy, with an upper limit of 22 mag arcsec⁻² in the *B* band. In fact, some low surface brightness features can be seen in the Legacy Survey DR10 image.

The Leo I group is well known for the Leo Ring which contains $1.7 \times 10^9 M_{\odot}$ of HI gas across a 225 kpc arc (Schneider 1989). It only contains a few isolated patches of optical emission, so is considered dark on a large scale. Taylor et al. (2022) study five dark HI clouds and one with a faint optical counterpart in this group with data from the Arecibo Galaxy Environment Survey (Auld et al. 2006). The sixth cloud has a smaller stellar mass ($M_{*} = 6.6 \times 10^6 M_{\odot}$) and HI to stellar mass ratio ($M_{\text{HI}}/M_{*} = 1.4$) than our almost dark cloud. These clouds all have significantly smaller HI masses and velocity widths than the one found in our system, with HI masses in the range $2.5\text{--}9 \times 10^6 M_{\odot}$ and velocity widths in the range $15 < w_{50} < 42 \text{ km s}^{-1}$. Although other formation mechanisms cannot be completely ruled out, like Klemola 13 and the NGC 3783 group, a tidal origin is favoured for all of the clouds. Three of the dark clouds are sandwiched between two spiral galaxies, M95 and M96, which have a projected separation of 136 kpc. Their proximity to the dark clouds, their similar velocities, and the warp seen in M96 suggests that the dark clouds are debris from a tidal interaction, despite there being no evidence of a tail.

Cannon et al. (2015) presented VLA follow-up observations of five almost dark objects from ALFALFA. Using their own analysis of the Sloan Digital Sky Survey (SDSS) images, rather than the results from the SDSS pipeline, they found that four of their sources did in fact have an extremely faint optical counterpart, like H1032 – 2819. However, H1032 – 2819 is so faint that the sensitivity of SDSS would

be too low to detect it, and it can not be seen in the Digitized Sky Survey image. Hence, Cannon et al. (2015) acknowledge that it is possible that deeper imaging could reveal an optical counterpart to the fifth object. Due to its location in the NGC 3370 group, they conclude that this object is also the result of tidal interactions rather than primordial, while the other four galaxies are most likely to be ‘failed’ galaxies with an extreme case of inefficient star formation. They have HI to stellar mass ratios ranging from 14 to 75 and *g*-band HI mass-to-light ratios ranging from 3 to 10, although Cannon et al. (2015) noted that deeper imaging would likely decrease the mass-to-light ratios of the other four objects. With the combination of new large HI and optical surveys such as WALLABY, the Legacy Survey archive, and the Rubin Observatory (Ivezić et al. 2019), we have entered an era when we can begin to probe the low surface brightness universe in a much more systematic manner.

6 SUMMARY AND CONCLUSIONS

A combination of WALLABY and archival ATCA data (López-Sánchez et al. 2008) has been used to perform an in-depth study of the almost dark cloud H1032 – 2819, and eight nearby galaxies (ESO 436 – G046, ESO 436 – IG042, ESO-LV 4360421, PGC 031288, PGC 031270, ESO 436 – G044, ESO 436 – G045, and ESO 437 – G004) in the interacting group Klemola 13 (also known as HIPASS J1034 – 28 and the Tol 9 group). We analysed the HI distribution as well as the kinematics of the system. H1032 – 2819 was first identified as a dark galaxy candidate in the VLA observations of McMahon (1993) and confirmed in Nançay observations by Duc et al. (1999). However, we have identified an extremely faint optical counterpart in data from the Legacy Survey DR10. The stellar mass-to-light ratio is $\Upsilon_{*} = 1.0 M_{\odot}/L_{\odot}$ and the estimated HI-to-stellar mass ratio is $M_{\text{HI}}/M_{*} = 7.6$ (using the WALLABY data). It has a mean *g*-band surface brightness of $27.0 \pm 0.3 \text{ mag arcsec}^{-2}$.

Like other dark, or almost-dark, galaxy candidates, H1032 – 2819 is unlikely to have a primordial origin (e.g. Kilborn et al. 2006; Taylor et al. 2022). The proximity of H1032 – 2819 to other galaxies in Klemola 13 makes a tidal origin likely. We have outlined two fly-by scenarios that give plausible explanations for the formation of the cloud. The fact that almost half of the HI in Klemola 13 is contained

in the intragroup medium, and that most of the member galaxies are H I deficient compared to the xGASS sample, supports this scenario.

The standard WALLABY source-finding pipeline (SoFiA) missed some extended gas in Klemola 13, but this was recovered with the use of bespoke SoFiA parameters which resulted in a larger mask. The peak column density is associated with ESO 436 – IG042. WALLABY was able to detect H I gas in two galaxies that ATCA did not (ESO 436 – G044 and ESO 436 – G045), although the ATCA data does show H I gas reaching towards these galaxies. ATCA was able to detect H I gas in one galaxy that WALLABY did not, PGC 031270.

The position of the cloud and Klemola 13 just inside the virial radius of Hydra Cluster suggests that ram pressure forces will probably drive future evolution, assuming that Klemola 13 is falling towards Hydra. As demonstrated by S_{rps} values consistently greater than 1, H1032 – 2819 and the intragroup gas are already susceptible to RPS, although the gas within the massive galaxies ESO 436 – G046 and ESO 347 – G004 is sufficiently anchored. The latter two galaxies are in regular rotation, allowing kinematic models and total mass estimates were derived using 3DBAROLO.

This paper showcases the potential of the full WALLABY survey to detect H I clouds and other extremely low surface brightness objects in the local Universe. WALLABY has a combination of column density sensitivity and angular resolution which allows easy cross-matching with optical/IR counterparts, even in the absence of spectroscopic data, and therefore easy identification of dark galaxy/cloud candidates. Further studies will concentrate on data from phase 2 of the pilot survey and the full WALLABY survey in combination with deep imaging data from the Legacy Survey.

ACKNOWLEDGEMENTS

We thank the anonymous referee for improving this manuscript.

This scientific work uses data obtained from Inyarrimanha Ilgari Bundara/the Murchison Radio-astronomy Observatory. We acknowledge the Wajarri Yamaji People as the Traditional Owners and native title holders of the Observatory site. CSIRO’s ASKAP radio telescope is part of the Australia Telescope National Facility (<https://ror.org/05qajvd42>). Operation of ASKAP is funded by the Australian Government with support from the National Collaborative Research Infrastructure Strategy. ASKAP uses the resources of the Pawsey Supercomputing Research Centre. Establishment of ASKAP, Inyarrimanha Ilgari Bundara, the CSIRO Murchison Radio-astronomy Observatory and the Pawsey Supercomputing Research Centre are initiatives of the Australian Government, with support from the Government of Western Australia and the Science and Industry Endowment Fund.

The ATCA is part of the Australia Telescope National Facility which is funded by the Australian Government for operation as a National Facility managed by CSIRO. We acknowledge the Gomerioi people as the traditional owners of the Observatory site.

Parts of this research were supported by the Australian Research Council Centre of Excellence for All Sky Astrophysics in 3 Dimensions (ASTRO 3D), through project no. CE170100013.

This investigation has made use of the NASA/IPAC Extragalactic Database (NED) which is operated by the Jet Propulsion Laboratory, California Institute of Technology, under contract with the National Aeronautics and Space Administration, and NASA’s Astrophysics Data System.

This publication makes use of data products from the Two Micron All Sky Survey, which is a joint project of the Univer-

sity of Massachusetts and the Infrared Processing and Analysis Center/California Institute of Technology, funded by the National Aeronautics and Space Administration and the National Science Foundation.

The Legacy Surveys consist of three individual and complementary projects: the Dark Energy Camera Legacy Survey (DECaLS; Proposal ID no. 2014B-0404; PIs: David Schlegel and Arjun Dey), the Beijing-Arizona Sky Survey (BASS; NAO Prop. ID no. 2015A-0801; PIs: Zhou Xu and Xiaohui Fan), and the Mayall z-band Legacy Survey (MzLS; Prop. ID no. 2016A-0453; PI: Arjun Dey). DECaLS, BASS, and MzLS together include data obtained, respectively, at the Blanco telescope, Cerro Tololo Inter-American Observatory, NSF’s NOIRLab; the Bok telescope, Steward Observatory, University of Arizona; and the Mayall telescope, Kitt Peak National Observatory, NOIRLab. Pipeline processing and analyses of the data were supported by NOIRLab and the Lawrence Berkeley National Laboratory (LBNL). The Legacy Surveys project is honored to be permitted to conduct astronomical research on Iolkam Du’ag (Kitt Peak), a mountain with particular significance to the Tohono O’odham Nation.

NOIRLab is operated by the Association of Universities for Research in Astronomy (AURA) under a cooperative agreement with the National Science Foundation. LBNL is managed by the Regents of the University of California under contract to the U.S. Department of Energy.

This project used data obtained with the Dark Energy Camera (DECam), which was constructed by the Dark Energy Survey (DES) collaboration. Funding for the DES Projects has been provided by the U.S. Department of Energy, the U.S. National Science Foundation, the Ministry of Science and Education of Spain, the Science and Technology Facilities Council of the United Kingdom, the Higher Education Funding Council for England, the National Center for Supercomputing Applications at the University of Illinois at Urbana-Champaign, the Kavli Institute of Cosmological Physics at the University of Chicago, Center for Cosmology and Astro-Particle Physics at the Ohio State University, the Mitchell Institute for Fundamental Physics and Astronomy at Texas A&M University, Financiadora de Estudos e Projetos, Fundacao Carlos Chagas Filho de Amparo, Financiadora de Estudos e Projetos, Fundacao Carlos Chagas Filho de Amparo a Pesquisa do Estado do Rio de Janeiro, Conselho Nacional de Desenvolvimento Cientifico e Tecnologico and the Ministerio da Ciencia, Tecnologia e Inovacao, the Deutsche Forschungsgemeinschaft and the Collaborating Institutions in the Dark Energy Survey. The Collaborating Institutions are Argonne National Laboratory, the University of California at Santa Cruz, the University of Cambridge, Centro de Investigaciones Energeticas, Medioambientales y Tecnologicas-Madrid, the University of Chicago, University College London, the DES-Brazil Consortium, the University of Edinburgh, the Eidgenossische Technische Hochschule (ETH) Zurich, Fermi National Accelerator Laboratory, the University of Illinois at Urbana-Champaign, the Institut de Ciencies de l’Espai (IEEC/CSIC), the Institut de Fisica d’Altes Energies, Lawrence Berkeley National Laboratory, the Ludwig Maximilians Universitat Munchen and the associated Excellence Cluster Universe, the University of Michigan, NSF’s NOIRLab, the University of Nottingham, the Ohio State University, the University of Pennsylvania, the University of Portsmouth, SLAC National Accelerator Laboratory, Stanford University, the University of Sussex, and Texas A&M University.

BASS is a key project of the Telescope Access Program (TAP), which has been funded by the National Astronomical Observatories of China, the Chinese Academy of Sciences (the Strategic Priority

Research Program ‘The Emergence of Cosmological Structures’ grant no. XDB09000000), and the Special Fund for Astronomy from the Ministry of Finance. The BASS is also supported by the External Cooperation Program of Chinese Academy of Sciences (grant no. 114A11KYSB20160057), and Chinese National Natural Science Foundation (grant nos 12120101003 and 11433005).

The Legacy Survey team makes use of data products from the Near-Earth Object Wide-field Infrared Survey Explorer (NEOWISE), which is a project of the Jet Propulsion Laboratory/California Institute of Technology. NEOWISE is funded by the National Aeronautics and Space Administration.

The Legacy Surveys imaging of the DESI footprint is supported by the Director, Office of Science, Office of High Energy Physics of the U.S. Department of Energy under contract no. DE-AC02-05CH1123, by the National Energy Research Scientific Computing Center, a DOE Office of Science User Facility under the same contract; and by the U.S. National Science Foundation, Division of Astronomical Sciences under contract no. AST-0950945 to NOAO.

PEMP acknowledges the support from the Dutch Research Council (NWO) through the Veni grant VI.Veni.222.364.

KS acknowledges support from the Natural Sciences and Engineering Research Council of Canada (NSERC).

PK is supported by the BMBF project 05A20PC4 for D-MeerKAT.

JR acknowledges funding from University of La Laguna through the Margarita Salas Program from the Spanish Ministry of Universities ref. UNI/551/2021-May 26, and under the EU Next Generation.

LVM acknowledges financial support from the grant CEX2021-001131-S funded by MCIN/AEI/ 10.13039/501100011033, from the grant PID2021-123930OB-C21 funded by MCIN/AEI/ 10.13039/501100011033, by ‘ERDF A way of making Europe’ and by the ‘European Union’.

DATA AVAILABILITY

The WALLABY source catalogue and associated data products (e.g. cubelets, moment maps, integrated spectra, and radial surface density profiles) are available online through the CSIRO ASKAP Science Data Archive (CASDA; Huynh et al. 2020) and the Canadian Astronomy Data Centre (CADC; Crabtree et al. 1994). All source and kinematic model data products are mirrored at both locations. Links to the data access services and the software tools used to produce the data products as well as documented instructions and example scripts for accessing the data are available from the WALLABY Data Portal.

This paper includes archived data obtained through the Australia Telescope Online Archive (<http://atoa.atnf.csiro.au>).

REFERENCES

- Auld R. et al., 2006, *MNRAS*, 371, 1617
 Bacchini C., Fraternali F., Iorio G., Pezzulli G., 2019, *A&A*, 622, A64
 Barnes D. G. et al., 2001, *MNRAS*, 322, 486
 Bekki K., Koribalski B. S., Kilborn V. A., 2005, *MNRAS*, 363, L21
 Bertin E., Arnouts S., 1996, *A&AS*, 117, 393
 Bílek M., Müller O., Vudragović A., Taylor R., 2020, *A&A*, 642, L10
 Bournaud F., Duc P. A., 2006, *A&A*, 456, 481
 Boylan-Kolchin M., Bullock J. S., Kaplinghat M., 2011, *MNRAS*, 415, L40
 Cannon J. M. et al., 2015, *AJ*, 149, 72
 Catinella B. et al., 2018, *MNRAS*, 476, 875
 Cornwell T. J., 2008, *IEEE J. Sel. Top. Signal Process.*, 2, 793
 Cornwell T., Humphreys B., Lenc E., Voronkov M., Whiting M., 2011, ASKAP-SW-0020: ASKAP Science Processing, ASKAP Science Case Memo Series 028, available at: <http://www.atnf.csiro.au/projects/askap/ASKAP-SW-0020.pdf>
 Crabtree D., Durand D., Fisher W., Gaudet S., Hill N., Justice G., Morris S., Woodsworth A., 1994, in Crabtree D. R., Hanisch R.J., Barnes J., eds, *Astronomical Data Analysis Software and Systems III*, A.S.P. Conference Series, Vol. 61. p. 123
 Davies J. et al., 2004, *MNRAS*, 349, 922
 Deg N. et al., 2022, *Publ. Astron. Soc. Aust.*, 39, e059
 Dey A. et al., 2019, *AJ*, 157, 168
 Di Teodoro E. M., Fraternali F., 2015, *MNRAS*, 451, 3021
 Disney M. J., 1976, *Nature*, 263, 573
 Disney M., Phillipps S., 1987, *Nature*, 329, 203
 Doyle M. T. et al., 2005, *MNRAS*, 361, 34
 Du W., Cheng C., Zheng Z., Wu H., 2020, *AJ*, 159, 138
 Duc P. A., Braine J., Lisenfeld U., Brinks E., Boquien M., 2007, *A&A*, 475, 187
 Duc P. A., Papaderos P., Balkowski C., Cayatte V., Thuan T. X., van Driel W., 1999, *A&AS*, 136, 539
 Duc P.-A., Bournaud F., 2008, *ApJ*, 673, 787
 Elagali A. et al., 2019, *MNRAS*, 487, 2797
 Erwin P., 2015, *ApJ*, 799, 226
 For B. Q. et al., 2021, *MNRAS*, 507, 2300
 Giovanelli R. et al., 2005, *AJ*, 130, 2598
 Gray L. M. et al., 2023, *AJ*, 165, 197
 Guzman J. et al., 2019, *Astrophysics Source Code Library*, record ascl:1912.003
 Haynes M. P. et al., 2018, *ApJ*, 861, 49
 Haynes M. P., Giovanelli R., Kent B. R., 2007, *ApJ*, 665, L19
 Hotan A. W. et al., 2021, *Publ. Astron. Soc. Aust.*, 38, e009
 Huynh M. et al., 2020, in Ballester P., Ibsen J., Solar M., Shortridge K., eds, *Astronomical Data Analysis Software and Systems XXVII*. ASP Conference Series, Vol. 522, Proceedings of a conference held (22-26 October 2017) at Sheraton Santiago Convention Center, Santiago de Chile, Chile. Astronomical Society of the Pacific, San Francisco, p. 263
 Iodice E. et al., 2020, *A&A*, 642, A48
 Iodice E. et al., 2021, *A&A*, 652, L11
 Iorio G., Fraternali F., Nipoti C., Di Teodoro E., Read J. I., Battaglia G., 2017, *MNRAS*, 466, 4159
 Ivezić Ž. et al., 2019, *ApJ*, 873, 111
 Janowiecki S. et al., 2015, *ApJ*, 801, 96
 Janowiecki S., Catinella B., Cortese L., Saintonge A., Brown T., Wang J., 2017, *MNRAS*, 466, 4795
 Jarrett T. H. et al., 2013, *AJ*, 145, 6
 Jarrett T. H., Cluver M. E., Taylor E. N., Bellstedt S., Robotham A. S. G., Yao H. F. M., 2023, *ApJ*, 946, 95
 Jiang F., Dekel A., Freundlich J., Romanowsky A. J., Dutton A. A., Macciò A. V., Di Cintio A., 2019, *MNRAS*, 487, 5272
 Jones D. H. et al., 2009, *MNRAS*, 399, 683
 Jones M. G., Bennet P., Mutlu-Pakdil B., Sand D. J., Spekkens K., Crnojević D., Karunakaran A., Zaritsky D., 2021, *ApJ*, 919, 72
 Kado-Fong E., Greene J. E., Huang S., Goulding A., 2022, *ApJ*, 941, 11
 Kamphuis P., Józsa G. I. G., Oh S. H., Spekkens K., Urbancic N., Serra P., Koribalski B. S., Detmar R. J., 2015, *MNRAS*, 452, 3139
 Kaviraj S., Darg D., Lintott C., Schawinski K., Silk J., 2012, *MNRAS*, 419, 70
 Kent B. R., 2010, *ApJ*, 725, 2333
 Kilborn V. A. et al., 2000, *AJ*, 120, 1342
 Kilborn V. A., Forbes D. A., Koribalski B. S., Brough S., Kern K., 2006, *MNRAS*, 371, 739
 Klemola A. R., 1969, *AJ*, 74, 804
 Klypin A., Kravtsov A. V., Valenzuela O., Prada F., 1999, *ApJ*, 522, 82
 Koda J., Yagi M., Yamanoi H., Komiyama Y., 2015, *ApJ*, 807, L2
 Koribalski B. S. et al., 2020, *Ap&SS*, 365, 118
 Kourkchi E., Tully R. B., 2017, *ApJ*, 843, 16
 Kravtsov A. V., 2013, *ApJ*, 764, L31
 La Marca A. et al., 2022, *A&A*, 665, A105

Lang R. H. et al., 2003, VizieR Online Data Catalog, p. J/MNRAS/342/738
 Lauberts A., 1982, ESO/Uppsala survey of the ESO(B) atlas. ESO, Garching
 Lee-Waddell K. et al., 2014, *MNRAS*, 443, 3601
 Leisman L. et al., 2017, *ApJ*, 842, 133
 Leisman L. et al., 2021, *AJ*, 162, 274
 Leisman L., Haynes M. P., Giovanelli R., Józsa G., Adams E. A. K., Hess K. M., 2016, *MNRAS*, 463, 1692
 Lelli F. et al., 2015, *A&A*, 584, A113
 Lim S. et al., 2020, *ApJ*, 899, 69
 Lin X. et al., 2023, *ApJ*, 956, 148
 López-Sánchez Á., Koribalski B. S., Esteban C., Hibbard J., 2008, in Jerjen H., Koribalski B. S.eds, *Galaxies in the Local Volume*. Springer Netherlands, Dordrecht, p. 301
 Mancera Piña P. E. et al., 2020, *MNRAS*, 495, 3636
 Mancera Piña P. E., Aguerri J. A. L., Peletier R. F., Venhola A., Trager S., Choque Challapa N., 2019, *MNRAS*, 485, 1036
 Mancera Piña P. E., Posti L., Fraternali F., Adams E. A. K., Oosterloo T., 2021, *A&A*, 647, A76
 Martin D. C. et al., 2005, *ApJ*, 619, L1
 Matsuoka Y., Ienaka N., Oyabu S., Wada K., Takino S., 2012, *AJ*, 144, 159
 McMahon P. M., 1993, PhD thesis, Columbia University, New York
 Meyer M. J. et al., 2004, *MNRAS*, 350, 1195
 Minchin R. et al., 2005, *ApJ*, 622, L21
 Oosterloo T., van Gorkom J., 2005, *A&A*, 437, L19
 Rau U., Cornwell T. J., 2011, *A&A*, 532, A71
 Reynolds T. N. et al., 2019, *MNRAS*, 482, 3591
 Reynolds T. N. et al., 2021, *MNRAS*, 505, 1891
 Reynolds T. N. et al., 2022, *MNRAS*, 510, 1716
 Robotham A. S. G., Bellstedt S., Lagos C. d. P., Thorne J. E., Davies L. J., Driver S. P., Bravo M., 2020, *MNRAS*, 495, 905
 Román J., Jones M. G., Montes M., Verdes-Montenegro L., Garrido J., Sánchez S., 2021, *A&A*, 649, L14
 Román J., Trujillo I., Montes M., 2020, *A&A*, 644, A42
 Sales L. V., Navarro J. F., Peñafiel L., Peng E. W., Lim S., Hernquist L., 2020, *MNRAS*, 494, 1848
 Sault R. J., Teuben P. J., Wright M. C. H., 1995, in Shaw R. A., Payne H. E., Hayes J. J. E.eds, *ASP Conf. Ser., Vol. 77, Astronomical Data Analysis Software and Systems IV*. Astron. Soc. Pac., San Francisco, p. 433
 Sawala T. et al., 2016, *MNRAS*, 457, 1931
 Schneider S. E., 1989, *ApJ*, 343, 94

Schneider S. E., Helou G., Salpeter E. E., Terzian Y., 1983, *ApJ*, 273, L1
 Serra P. et al., 2015, *MNRAS*, 448, 1922
 Skrutskie M. F. et al., 2006, *AJ*, 131, 1163
 Taylor E. N., Webster R. L., 2005, *ApJ*, 634, 1067
 Taylor R. et al., 2022, *AJ*, 164, 233
 Taylor R., Davies J. L., Jáchym P., Keenan O., Minchin R. F., Palouš J., Smith R., Wunsch R., 2016, *MNRAS*, 461, 3001
 van der Burg R. F. J., Muzzin A., Hoekstra H., 2016, *A&A*, 590, A20
 van Dokkum P. G., Abraham R., Merritt A., Zhang J., Geha M., Conroy C., 2015, *ApJ*, 798, L45
 Verde L., Oh S. P., Jimenez R., 2002, *MNRAS*, 336, 541
 Wang J. et al., 2021, *ApJ*, 915, 70
 Wang S. et al., 2022, *ApJ*, 927, 66
 Westmeier T. et al., 2021a, *Astrophysics Source Code Library*, record ascl:2109.005
 Westmeier T. et al., 2021b, *MNRAS*, 506, 3962
 Westmeier T. et al., 2022, *PASA*, 39, e058
 Whiting M. T., 2020, in Ballester P., Ibsen J., Solar M., Shorridge K.eds, *ASP Conf. Ser., Vol. 522, Astronomical Data Analysis Software and Systems XXVII*. Astron. Soc. Pac., San Francisco, p. 469
 Wieringa M., Raja W., Ord S., 2020, in Pizzo R., Deul E. R., Mol J. D., de Plaa J., Verkouter H.eds, *ASP Conf. Ser., Vol. 527, Astronomical Data Analysis Software and Systems XXIX*. Astron. Soc. Pac., San Francisco, p. 591
 Wong O. I. et al., 2021, *MNRAS*, 507, 2905
 Wright E. L. et al., 2010, *AJ*, 140, 1868
 Zaritsky D., Donnerstein R., Karunakaran A., Barbosa C. E., Dey A., Kadowaki J., Spekkens K., Zhang H., 2022, *ApJS*, 261, 18

APPENDIX A: KINEMATIC MODELS

In this section, we present the kinematic models of ESO 436 – G046 and ESO 437 – G004 created using 3DBAROLO (Di Teodoro & Fraternali 2015). The software models the HI gas as 3D tilted rings, fitting for rotation velocity, inclination, and position angle, which can be seen in Figs A1(b) and A2(b). The red points in these figures are the final results, while the grey are the outputs of the first iteration. Figs A1 and A3(a) shows the relevant outputs for ESO

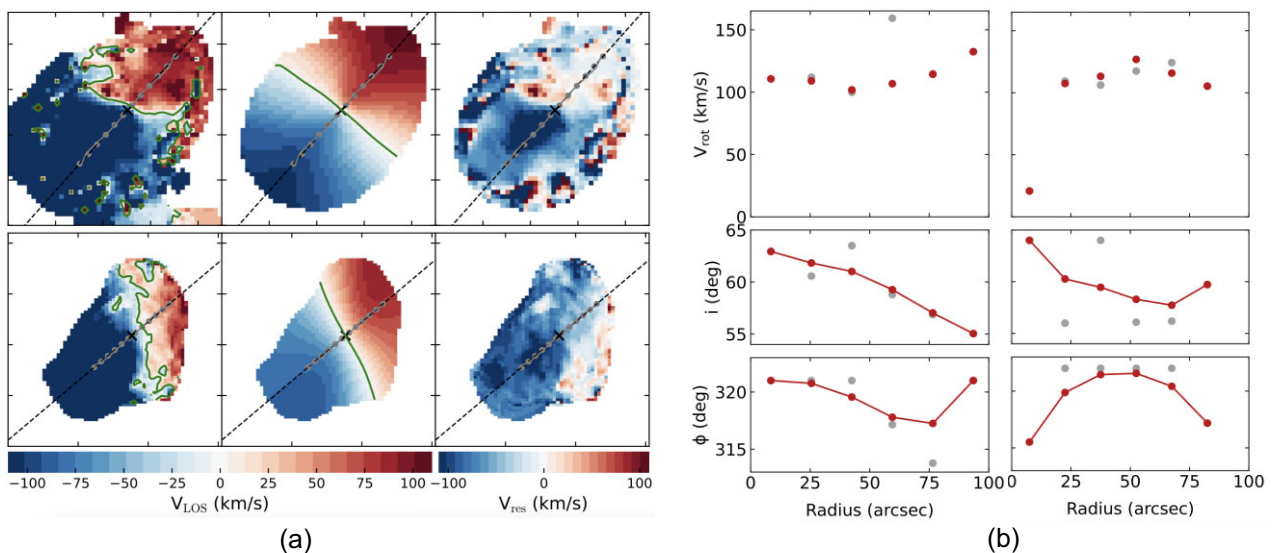


Figure A1. 3DBAROLO models for ESO 437 – G004 using WALLABY and ATCA data. (a) 3DBAROLO moment 1 maps. Top row: WALLABY, bottom row: ATCA. Left column: data, middle column: model, right column: residuals. The green contours show where the line of sight velocity is equal to zero. (b) 3DBAROLO parameter fits. Left column: WALLABY, right column: ATCA. Top row: rotation velocity, middle row: inclination, bottom: position angle.

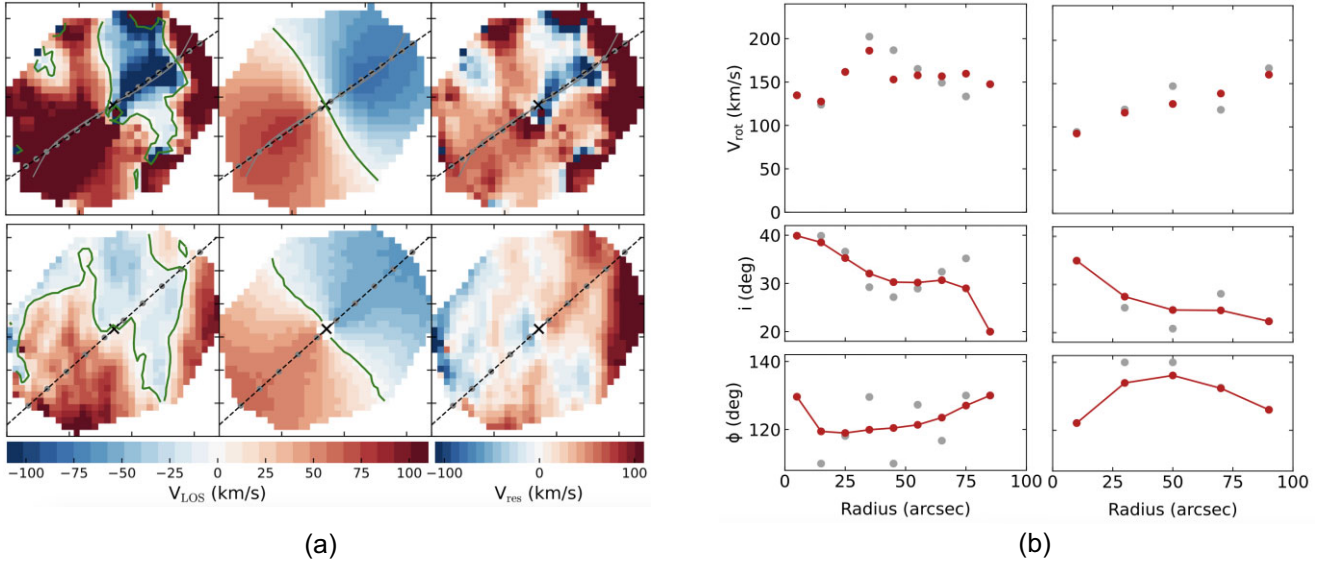


Figure A2. 3DBAROLO models for ESO 436 – G046 using WALLABY and ATCA data. (a) 3DBAROLO moment 1 maps. Top row: WALLABY, bottom row: ATCA. Left column: data, middle column: model, right column: residuals. The green contours show where the line of sight velocity is equal to zero. (b) 3DBAROLO parameter fits. Left column: WALLABY, right column: ATCA. Top row: rotation velocity, middle row: inclination, bottom: position angle.

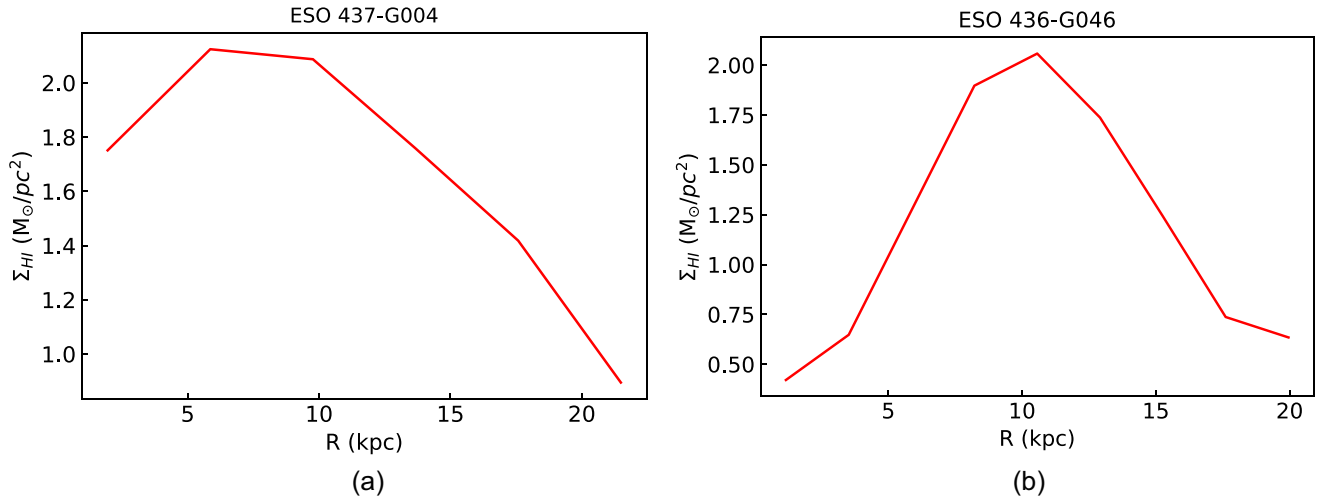


Figure A3. The H I mass surface density profiles for ESO 437 – G004 (left) and ESO 436 – G046 (right) from the 3DBAROLO kinematic models. The WALLABY data were used.

437 – G004 and Figs A2 and A3 (b) show those of ESO 436 – G046. The H I mass surface density estimated by these kinematic models for the WALLABY data was used in the calculation of S_{rps} in Fig. 7(b).

It is worth noting here that the models are very sensitive to the initial estimates. To demonstrate this, alternative models for the WALLABY and ATCA data of ESO 437 – G004 are shown in Fig. A4. In the original models, roughly two rings are fit per beam, as done in the WALLABY kinematic modelling pipeline (Deg et al. 2022) and in previous WALLABY studies (Elagali et al. 2019; Reynolds et al. 2019). However, in the alternative models, the radial separation of the rings is increased to reduce the effects of oversampling. Additionally, these alternative models hold a fixed inclination and position angle, and fit for the rotation and dispersion velocity, whilst the original models fit for position angle, inclination, and rotation velocity and hold the dispersion velocity fixed. Finally, the alternative

models allow 3DBAROLO to find its own mask in the already masked cube. These changes to initial conditions result in rotation velocities of ~ 220 and ~ 210 km s^{-1} for the WALLABY and ATCA data, respectively. Not only is this significantly higher than the rotation velocities of the original model, but also is significantly higher than the WKAPP value. If we use the results of the alternative models, then the extended gas of ESO 437 – G004 would be far less susceptible to RPS. On average, the residuals of the alternate models are a factor of ~ 3 lower than those of the original models. The impact of changing the initial conditions is not unexpected, as Kamphuis et al. (2015) found that kinematic modelling for observations with fewer than eight beams will likely lead to large degeneracies in parameters and loose constraints. Hence, future deeper and higher resolution observations are likely to improve our constraints on the kinematic modelling.

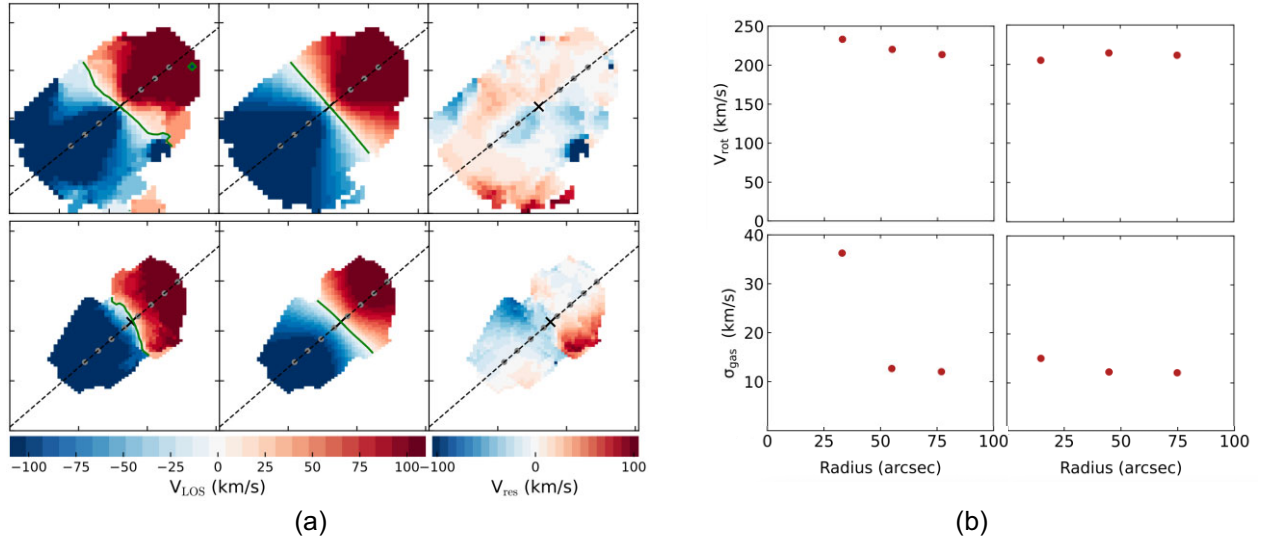


Figure A4. Alternative 3DBAROLO models for ESO 437 – G004 using WALLABY and ATCA data. (a) 3DBAROLO moment 1 maps. Top row: WALLABY, bottom row: ATCA. Left column: data, middle column: model, right column: residuals. The green contours show where the line of sight velocity is equal to zero. (b) 3DBAROLO parameter fits. Left column: WALLABY, right column: ATCA. Top row: rotation velocity, bottom: velocity dispersion. The inclinations are set to 40° and the position angles are set to 310° and 320° for WALLABY and ATCA respectively.

APPENDIX B: STELLAR MASS AND SPECIFIC STAR FORMATION RATE

The values used in the calculations of the stellar mass and sSFR in Section 4.3 are shown in Table B1. The references for this data and the equations used are presented in Section 4.3.

Table B1. The quantities used in the calculations of stellar mass and sSFR in Section 4.3. The rows from top to bottom are: *GALEX* NUV flux density, *W1 WISE* magnitude, *W2 WISE* magnitude, *W3 WISE* magnitude, and *W4 WISE* magnitude.

Parameter	ESO 436-G046	ESO 436-IG042	ESO-LV 4360421	PGC 031288	PGC 031270	ESO 436-G044	ESO 436-G045	ESO 437-G004
F_{NUV} (μJy)	8686 ± 45	771 ± 20	–	7 ± 3	224 ± 7	95 ± 6	37 ± 4	947 ± 17
m_{W1} (mag)	11.23 ± 0.02	11.11 ± 0.02	13.40 ± 0.02	11.30 ± 0.02	12.81 ± 0.02	10.33 ± 0.02	11.25 ± 0.02	11.42 ± 0.02
m_{W2} (mag)	11.26 ± 0.02	10.74 ± 0.02	13.42 ± 0.03	11.37 ± 0.02	12.78 ± 0.03	10.38 ± 0.02	11.34 ± 0.02	11.38 ± 0.02
m_{W3} (mag)	–	–	–	10.68 ± 0.09	–	–	10.78 ± 0.09	–
m_{W4} (mag)	6.02 ± 0.04	3.31 ± 0.03	8.56 ± 0.34	–	7.02 ± 0.08	8.31 ± 0.26	–	5.79 ± 0.05

¹*International Centre for Radio Astronomy Research (ICRAR), The University of Western Australia, 35 Stirling Highway, Crawley, WA 6009, Australia*

²*ARC Centre of Excellence for All Sky Astrophysics in 3 Dimensions (ASTRO 3D), Australia*

³*CSIRO Space & Astronomy, PO Box 1130, Bentley, WA 6102, Australia*

⁴*Centre for Astrophysics and Supercomputing, Swinburne University of Technology, Hawthorn, Victoria 3122, Australia*

⁵*International Centre for Radio Astronomy Research (ICRAR), Curtin University, Bentley, WA 6102, Australia*

⁶*Leiden Observatory, Leiden University, PO Box 9513, NL-2300 RA Leiden, The Netherlands*

⁷*Kapteyn Astronomical Institute, University of Groningen, PO Box 800, NL-9700 AV Groningen, The Netherlands*

⁸*Departamento de Astrofísica, Universidad de La Laguna, E-38206, La Laguna, Tenerife, Spain*

⁹*Instituto de Astrofísica de Andalucía (IAA-CSIC), Glorieta de la Astronomía s/n, 18008 Granada, Spain*

¹⁰*Department of Physics, Engineering Physics, and Astronomy, Queen’s University, Kingston, ON, K7L 3N6, Canada*

¹¹*School of Physical Sciences and Nanotechnology, Yachay Tech University, Hacienda San José S/N, 100119 Urcuquí, Ecuador*

¹²*Faculty of Physics and Astronomy, Astronomical Institute (AIRUB), Ruhr University Bochum, D-44780 Bochum, Germany*

¹³*CSIRO Space & Astronomy, Australia Telescope National Facility, PO Box 76, NSW 1710, Australia*

¹⁴*School of Science, Western Sydney University, Locked Bag 1797, Penrith, NSW 2751, Australia*

¹⁵*Department of Physics and Space Science, Royal Military College of Canada, PO Box 17000, Station Forces, Kingston, ON K7K 7B4, Canada*

¹⁶*Kavli Institute for Astronomy and Astrophysics, Peking University, Beijing 100871, China*

¹⁷*School of Mathematical and Physical Sciences, Macquarie University, NSW 2109, Australia*

¹⁸*Research Centre for Astrophysics and Space Technologies, Macquarie University, NSW 2109, Australia*

This paper has been typeset from a $\text{\TeX}/\text{\LaTeX}$ file prepared by the author.